2017

ANALYSIS OF AEROELASTIC EFFECTS ON THE 3-DIMENSIONAL INTERFERENCE OF WIND-TURBINE ROTORS

Anurag Rajan
Michigan Technological University, arajan@mtu.edu

ANALYSIS OF AEROELASTIC EFFECTS ON THE 3-DIMENSIONAL INTERFERENCE OF WIND-TURBINE ROTORS

By

Anurag Rajan

A DISSERTATION

Submitted in partial fulfillment of the requirements for the degree of

DOCTOR OF PHILOSOPHY

In Mechanical Engineering - Engineering Mechanics

MICHIGAN TECHNOLOGICAL UNIVERSITY

2017

This dissertation has been approved in partial fulfillment of the requirements for the Degree of DOCTOR OF PHILOSOPHY in Mechanical Engineering - Engineering Mechanics.

Department of Mechanical Engineering - Engineering Mechanics

Dissertation Advisor: *Dr. Fernando Ponta*

Committee Member: *Dr. Jeffery Allen*

Committee Member: *Dr. Leonard Bohmann*

Committee Member: *Dr. Lucia Gauchia*

Department Chair: *Dr. William W. Predebon*

Contents

List of Figures

List of Tables

Abstract

Greater penetration of wind energy demands better utilization of available wind. This has led to a formidable increase in the rotor diameter over the past few years. Bigger rotors call for lighter, more flexible blades to reduce loads and improve fatigue life. As a result, future blades will deform substantially more than the relatively stiff blades of the past. More efficient use of wind power also calls for incorporating advanced active and passive control strategies and increasing the range of velocities over which wind energy is captured. Hence an improvement in the quality of numerical simulations capable of capturing the effects of these deformations is key to innovations in wind-turbine technology.

The code on which this research aims to improve upon is called the Dynamic Rotor Deformation - Blade Element Momentum model (DRD-BEM) introduced by Ponta et al. [8]. It combines an advanced structural model with an aerodynamic model implemented in a parallel HPC supercomputer platform. The structural part simulates the response of heterogeneous composite blades, based on a variation of the dimensional reduction technique proposed by Hodges and Yu Yu et al. [12]. This approach reduces the 3-Dimensional complexity of the blade section into a stiffness matrix for an equivalent beam, substantially reducing the computational effort required to model the structural dynamics at every time step. The aerodynamic model is based on an

advanced implementation of the Blade Element Momentum (BEM) theory, where all velocities and forces are re-projected into the deformed configuration at that instant. This ensures that the effects of all the complex modes of rotor deformation and subsequent rotation of airfoil sections are accounted for while computing the aerodynamic forces.

As a result of the out of plane attitudes of the rotor sections introduced by blade deformations and various control strategies the hitherto small radial component of aerodynamic forces in the hub must now be taken into account. In this research we present a way to extend the capabilities of DRD-BEM by taking into consideration the 3-Dimensional effects of these forces on rotor interference. In this method, called the 3-D DRD-BEM, the coordinate system where the momentum balance is performed in BEM theory is moved, from the hub, to the instantaneous position and alignment of the blade section in its deformed configuration. Another aspect that becomes important as blades become more flexible and control strategies become more complex, is the high axial induction factor regime of turbine operation. This becomes more evident in the instaneous blade section coordinate system of the 3-D DRD-BEM. In most implementations of BEM, this flow regime is modeled using empirical relations based on experimental data with no consensus on which empirical relation to use. This research uses CFD solutions to develop an improved actuator disk model and revisit the above mentioned experiments for a more accurate representation of these operational states.

Chapter 1

Introduction

Worldwide demand for energy has been steadily increasing especially in developing countries like India, China and Brazil. This has lead to a renewed interest in developing renewable sources of energy like wind and solar to reduce the environmental impact caused by conventional methods of generating electricity. Wind energy has emerged as an important supplier of grid-connected electricity in the global energy picture thanks to considerable technological progress during the last twenty years [13]. Wind power is one of the most rapidly growing renewable energies. Global installed capacity grew from 14,604 MW in 2000 to 84,934 MW in 2007, an impressive rate of 482% in only seven years according to [14]. In 2016 wind energy emerged ahead of coal and nuclear as the second largest source of power in Europe after gas. The Global Wind Energy Council in its Global Wind Energy Outlook 2016 have outlined

scenarios where wind could supply 20% of global electricity by 2030.

This rapid spread of wind energy has fueled the need for constant innovation in the wind-turbine industry. Current trends clearly show a steady increase in size of state-of-the-art wind turbines. The European Wind Energy Association (EWEA) in a recent report have predicted state-of-the-art turbines capable of generating 20 MW with rotor diameters in excess of 250 m [15]. In a study carried out by the swiss federal institute of technology it has been suggested that over the last three decades, the size of the state-of-the-art machine has increased four times. Economies-of-scale factors drive this tendency substantially reducing the cost of wind energy. Some of the largest wind turbines in operation are Vestas V164 8MW, Enercon E126 7.5MW, Samsung S7.0 171 7MW , Siemens SWT-7.0-154 and REpower 6M 6.2MW. Figure 1.1 shows the 7 MW Siemens SWT 7.0 154.

Such huge rotors lead to much higher loads on turbine blades increasing the need for developing lighter and hence more flexible blades along with new and complex control strategies. However, with increasing rotor sizes and numerous innovative control strategies to be explored extrapolating experimental data becomes increasingly complicated, expensive and time consuming. The need for mathematical models that can act as virtual laboratories has never been felt more in the wind turbine industry than the present. Simulation models are increasingly being used for optimizing the structural as well as aerodynamic aspects of wind turbines. However, the complexity

Figure 1.1: Siemens 7MW Wind turbine With a rotor diameter of 154 meters. (Photo: www.siemens.com/press, Appendix B)

of these innovations added to the already complex coupled aeroelastic problem of wind turbine dynamics pushes the limits of existing computer models. As mentioned above, upscaling has led to higher loads as well as increased cost of manufacture, and, therefore, has prompted the need to design lighter, more flexible blades. New control mechanisms exploiting this increase in flexibility have been proposed and studied in the form of *adaptive blades*, which utilize coupling between bending and twisting to reduce extreme loads and improve the fatigue performance of these mega structures (for a detailed discussion on the adaptive-blade concept see [16] and references within). Coning rotors is another promising innovation that could be used to mitigate the effects of extreme loads and improve energy capture (see Jamieson [17]). Crawford and Platts [18] present a detailed discussion of the development and operation of coned rotors. Rasmussen et al. [19] introduced a downwind soft rotor concept. This rotor concept is expanded further in the form of a segmented blade design, which hinges at a joint [20] (see figure 1.2) or joints at multiple segments [21], to align the rotor with the wind direction under extreme conditions. It is clear that these novel approaches will introduce much higher levels of misalignments of blade sections with respect to the plane of rotation than what has been seen hitherto. The rotor configuration will, therefore, differ significantly from the original one on which most of the hypotheses of existing models are based. Some of the underlying assumptions in these hypotheses must now be re-evaluated to account for the above mentioned changes. An important example is Crawford's analysis of the applicability of the BEM theory for the coning

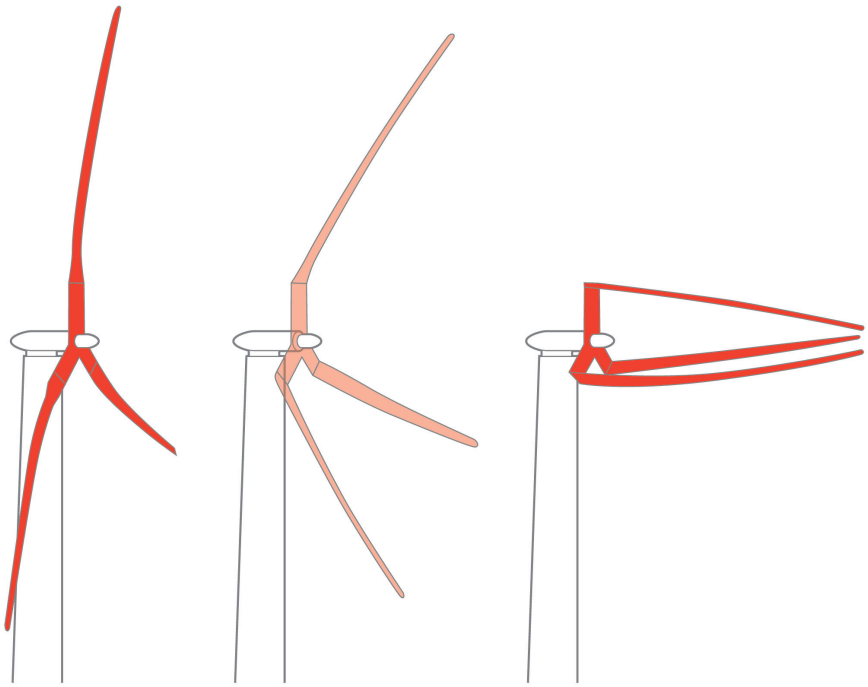

Figure 1.2: A Segmented Ultralight Morphing Rotor (SUMR) from Sandia National Laboratories. A concept 50-MW turbine which can stow away the blades under extreme conditions by aligning them with the wind direction to prevent damage to the rotor. The blades can be spread out again in low winds to maximize energy capture. (Illustration by TrevorJohnston.com / Popular Science [1], Appendix B)

rotors mentioned above [22]. All of this, as explained in the next section, forms the basis of this dissertation.

1.1 Dissertation goals

Existing codes couple the aerodynamic and structural models either as a full 3D problem (see Bazilevs et al. [23, 24] for more details) or after using some form of dimensional reduction. Full 3-D models being computationally expensive, limit the number

of new turbine designs and control strategies that can be tested. Dimensionally reduced schemes can, however, represent critical features of the coupled multi-physics dynamics of the aeroelastic problem, with much less computational effort.

For the structure of the blade, once it has been reduced dimensionally to a 1-D problem, its behavior is usually modeled using either the Bernoulli theory or the more comlex Timoshenko beam theory. The problem is then solved using either a spatial discretization method (like finite elements or finite differences) or a modal discretization scheme which keeps only a finite number of deformation modes in the solution. In both methods continuity also reduces to a 1-D domain. For solving the aerodynamics involved in an aeroelastic problem, generally the classical Blade Element Momentum (BEM) theory is implemented. Together the structural and aerodynamic models provide a coupled, non-linear scheme (see [25] for a comprehensive explanation). Most existing models like the FAST-Aerodyn suite [26, 27, 28] are based on such a technique. These combined models while quite successful do not effectively capture the entire range of interactions between the structural and aerodynamic parts of the model. The mutual feedback between the two, in the form of rorotr deformation from the structural side effecting aerodynamic loads and the aerodynamic loads from the flow model in turn effecting rotor deformation, has a very limited representation in these models. To better capture this complex interaction and for a higher level of description, a complex simulation model combining two advanced numerical

schemes was developed. It consists of a mathematical model for the structural response [29] based on a dimensional reduction technique proposed by Yu et al. [12]. The model is able to capture and couple all deformation modes of a heterogeneous composite wind turbine blade, while saving significantly computational expense. The aerodynamic part uses an innovative BEM approach with orthogonal transformation matrices, constructed using the instantaneous deformed configuration of a blade section, used to reproject velocities and force vectors at that section. This model is able to incorporate the effects of deformation on the aerodynamic loads and vice versa at every instant. This advanced aeroelastic model is called the Dynamic Rotor Deformation - Blade Element Momentum model (DRD-BEM) (see Ponta et al. [8]).

However, further exploration is required when dealing with future turbines using different control techniques and flexible blades increasing the complexity of the aeroelastic problem. All existing models using the BEM principle consider only the axial and tangential force components in the hub coordinate system. This work aims at including the effects of the radial force component to the DRD-BEM model. The radial forces will have increasing significance with the introduction of flexible pre-conformed blades and innovative control strategies leading to rapidly varying blade attitudes.

With widespread implementation of adaptive blade strategies (for details see [16]) and active control mechanisms, turbine rotors can be expected to undergo higher levels of distortion and also remain operational for a much wider range of wind velocities.

All these factors often lead to certain blade sections encountering operational states, possibly in the midst of a control action, with axial induction factors greater than 0.5. A few possible scenarios which could drive blade sections into this regime are:

1. Transitional states during control actions, e.g. pitch-to-feather, reducing rotor RPM against rotor inertia etc. [30, 31].
2. Operating in part load conditions during high wind conditions to store and release kinetic energy of rotating masses as required [32, 33, 34, 35, 36, 37].
3. Sudden drop in effective or actual wind speeds [38]
4. Failure of control actions
5. Deformation of blades, as they become increasingly flexible, might drive certain sections into such regimes.

Sebastian [38] presents an analysis of how often off-shore wind turbines can enter such regimes. The assumptions of the momentum theory across a stream tube as used in BEM cannot be used in this regime. In most implementations of BEM, this high axial induction factor flow regime is modeled using empirical relations based on experimental data.

The empirical relations were first proposed by Glauert [4] wherein he considered data from [7, 11, 39]. Several modifications have been proposed to this empirical

fitting of the experimental data as seen in [2, 5, 16, 40]. These modifications will be briefly discussed in subsequent sections. There is no clear consensus on which relation best describes this flow regime. One of the reasons could be the uncertainty in the experimental results especially in the vortex ring state. The original data has a lot of dispersion due to limitations of sensors used in that era as well as the unsteady nature, as expected, of a non-ideal case. The BEM theory, on the other hand, is based on a steady in the average momentum balance across an ideal actuator disk.

The goal of this dissertation can therefore be divided into two phases:

1. First, to develop a BEM model capable of implementing the effects of the above-mentioned radial forces in the momentum balance, giving a full 3-Dimensional representation to the rotor interference.

2. Second, a more accurate representation of the various high axial induction factor operational states mentioned above in our BEM model (3-D DRD BEM). For this, it would be useful to further explore these regimes, using a CFD tool to solve for flow across an exact representation of an actuator disk instead of relying solely on the above mentioned experimental data.

It should be noted that the REPower 5M shown in Figure 1.3 forms the basis of the reference turbine used in this research. It can generate 5 MW with a rotor diameter of 126 m (see basic characteristics on table 1.1) being available for both inland and

Figure 1.3: REpower 5M, with an output power of 5 MW and a rotor diameter of 126 m. Picture taken by Hans Hillewaert. Appendix B.

offshore installations.

Table 1.1
Main characteristics of the REpower 5MW wind turbine.

Design	
Rated Power	5000 kW
Cut-In Wind Speed	3.5 m/s
Rated Wind speed	13 m/s
Cut-Out Wind Speed	
Offshore Version	30 m/s
Onshore Version	25 m/s
Rotor	
Diameter	126 m
Speed Range	6.9–12.1 rpm
Blades	
Length	61.5 m

1.2 Dissertation Outline

Chapter 2 presents the theoretical background of the standard DRD-BEM model. It couples the aerodynamic and structural models as a dimensionally reduced one dimensional model. Full 3-D models being computationally expensive, limit the number of new turbine designs and control strategies that can be tested. The dimensionally reduced scheme used in DRD-BEM can represent critical modes of deformation of the complex aeroelastic problem, with reduced computational effort.

DRD-BEM models the structural response by using the Generalized Timoshenko Beam Model (GTBM). The GTBM is a generalized implementation of the Timoshenko beam theory using a variational asymptotic method. It accounts for warping of beam sections by interpolating sectional warping using a 2-D Finite element model

to obtain 3-D warping functions. These warping functions are used to asymptotically approximate the 3-D strain energy at each section in terms of the six strain measures including those of the classical 1-D Timoshenko theory and the transverse shear in two directions. The complex geometry and material properties are represented by stiffness matrices obtained a priori for each section. The generalized implementation of the Timoshenko theory ensures a fully populated 6x6 stiffness matrix at each section of the beam coupling all 6 modes of deformation. The 3-D beam problem is thus reduced to a nonlinear 1-D beam. This unsteady nonlinear 1-D beam problem together with the aerodynamic aspect discussed later comprises the aeroelastic problem. This aeroelastic problem is solved along the beam's reference axis, L, for every time step using an advanced ODE algorithm. From each time step of the ODE solution the 3-D fields can be recovered using the previously derived 3-D warping functions. As seen in figure 2.1 the solution variables first represented in a coordinate system along L are transformed into the instantaneous coordinate system along the new configuration l. This is done with the help of the C_{Ll} matrices, updated at every time step of the ODE solution of the structural model. Thus the instantaneous position of each blade section is accurately tracked by this intrinsic coordinate system. As a result the aerodynamic part of the aeroelastic analysis gets this updated information at every time step for each blade section. At the same time the results of the aerodynamic solution constantly update the aerodynamic loads acting at each blade section as inputs to the structural model for every time step. This is the original DRD-BEM model which

this dissertaion aims to improve upon in the form of the 3-D DRD-BEM as explained in chpater 3.

Chapter 3 presents the new 3-D DRD-BEM model. As mentioned earlier, there are still aspects that need further exploration, especially in case of future turbines using different control techniques or characterized by complex modes of deformation. Hitherto, all models based on the BEM principle have considered the axial and tangential component of forces acting on the system of coordinates of the rotor hub. What the present work introduces to the DRD-BEM model, is the radial component. The radial force component will have increasing implications with the introduction of flexible pre-conformed blades, as increased flexibility, along with rapidly varying blade attitudes (both important aspects of wind turbine control), have a noticeable effect on the radial forces. Hence, it becomes important to include the effects of these forces in the momentum balance of a BEM implementation, giving a full 3-Dimensional representation to the rotor interference. This is essentially the 3-D DRD-BEM model presented in this thesis.

Chapter 4 presents the numerical experimentation designed to analyze the 3-D DRD-BEM model. These experiments are performed on a reference turbine model called the NREL 5-MW reference wind turbine developed by NREL [41]. This reference turbine is based on the REPower 5M shown in Figure 1.3. It can generate 5 MW with a rotor diameter of 126 m (see table 1.1) being available for both inland and

offshore installations and is well representative of typical utility-scale multi megawatt commercial wind turbines. The numerical experiments consists of comparing the original DRD-BEM model with the 3-D DRD-BEM model by varying certain aspects of the rotor model including conicity, tilt and blade stifness. The effect of these variations on variables like power, thrust, tip-displacement etc are analyzed as a means to compare the two models.

Chapter 5 explains the need to revisit the set of experimental data used in BEM as part of Glauert correction for high axial induction factor regimes. This is done with the help of an actuator disk model in Fluent. This new set of numerical data is then used to define a new empirical curve which can be used to find the thrust at high induction factors. It then goes on to presesnt a set of experiments designed to test this new empirical curve as part of the new 3-D DRD-BEM model. With the help of these experiments the importance of exploring these regimes is highlighted.

Finally, chapter 6 presents the conclusions for this dissertation work as well as the outlook for further work based on the analysis of the material presented in the previous chapters

Chapter 2

Dynamic Rotor Deformation - Blade Element Momentum Model

2.1 Introduction

The two predominant yet distinct approaches to numerical simulation of horizontal axis wind turbines are the stream-tube and the vortex modeling approaches. The stream-tube model known widely as the BEM model, proposed almost a century ago [4, 42], is the most widely used aerodynamic component for analyzing wind turbine rotors (see [43] and [2] for a comprehensive description of classical BEM). Over the pat few decades there have been several improvements and corrections to classical BEM .

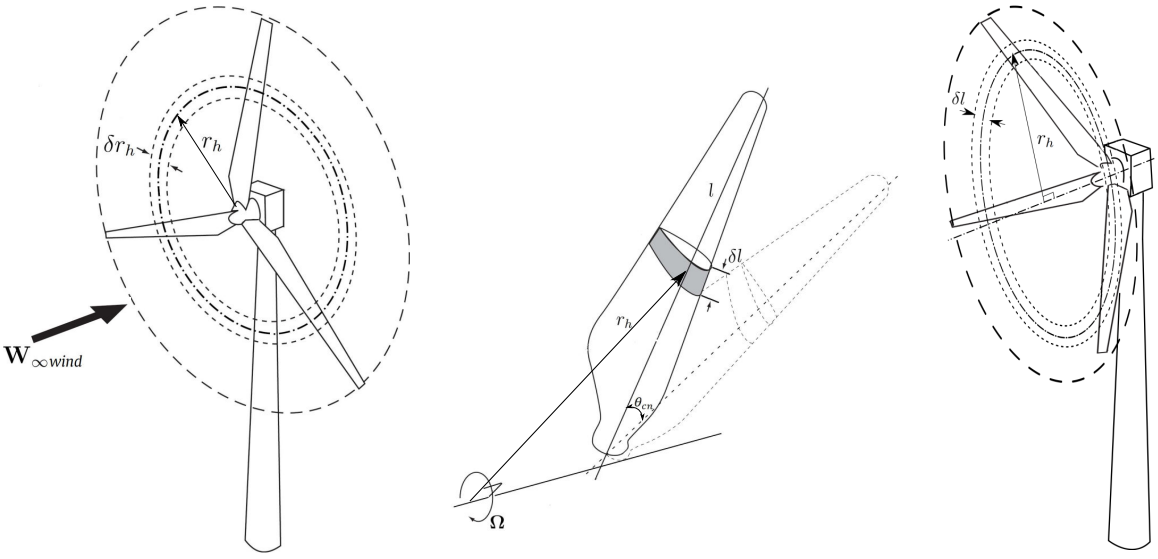

Figure 2.1: A schematic showing the sweeping out of an annular actuator by a blade element (based on the classical BEM representation schematic in Burton et al. [2]) with and without coning.

Some examples of such modifications over the last decade include works of: Crawford [22] concerned with analyzing BEM for coning rotors, Lanzafame and Messina [44] which analyzed and proposed mathematical models representing lift and drag coefficients. Lanzafame and Messina [45] which explored inclusion of centrifugal pumping into the BEM model therby modifying lift. Madsen et al. [46] which was concerned with modifications based on a detailed analysis of numerical and analytical results of several aerodynamic models. Dai et al. [47] involved corrections to the dynamic stall model proposed by Leishman and Beddoes [48]. Vaz et al. [49] included into the BEM model, the effects of wake influence.

The trigonometric projections of velocities and forces used in the classical implementation of BEM are made under the assumption that the blade sections remain

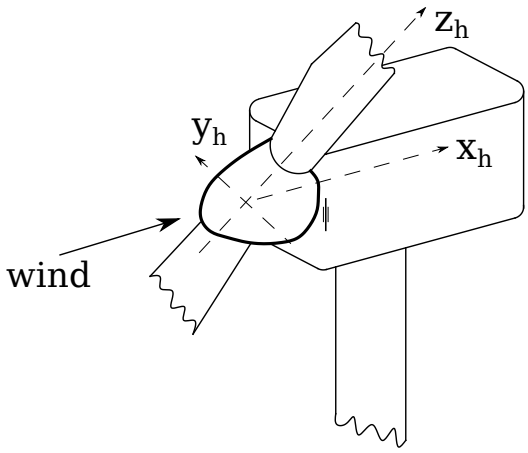

Figure 2.2: The hub coordinate system in accordance with the International Electrotechnical Commission (IEC) standards [3]

perpendicular to the radial plane of the rotor. Therefore, sectional misalignments as a result of larger deformations seen in modern wind turbine rotors are not accounted for while calculating aerodynamic forces. In fact, even the area of the annular actuator disk is misrepresented since the blade section deformation changes the thickness of the corresponding stream-tube. These deformations are, however, efficiently captured in the DRD-BEM model where the incident velocity and the aerodynamic forces are transformed through different coordinate systems using a set of orthogonal matrices. The transformations include all the misalignments starting from the coordinate system aligned with the incident wind up to that aligned with the final deformed configuration of that section at any given instant. The misalignments can be a result of blade section deformation, control actions like pitching and yawing, azimuthal rotation, wind direction changes or even design features like coning-angle or tilt.

Figure 2.1 represents the instantaneous position of a blade element at radius r_h with

respect to the hub. δl is the the spanwise length of the blade element and when projected onto the hub-coordinate system (figure 2.2) it gives the radial thickness of the annular actuator as swept out by that element. As mentioned earlier, DRD-BEM takes in to account all possible misalignments at every instant. This ensures that the area swept by the blade element is updated constantly in the h-coordinate system. At this point, It should be noted that before deflection, the stream tube is aligned with with the incident wind and not the hub, owing to the action of the orthogonal matrices. At the actuator it gets deflected by the forces exerted on the wind by the actuator. The coned rotor schematic in the extreme right of figure 2.1 shows how the thickness of the annular actuator swept by a particular blade section in a coordinate system aligned with that section is given by $r_h \delta l$. This detail is important for developing equations for phase A of this research, as explained in the next chapter.

2.2 Blade structural model: The dimensional-reduction technique for beams

Blades of a Wind turbine can be modeled as slender beams saving computational expense in comparison with a full 3-D analysis. However, traditional beam theories (Bernoulli or standard Timoshenko) do not take into account complex internal structures or heterogeneous distribution of material properties (see figure 2.3, showing a

typical internal structure of a wind turbine blade. More details on the internal structure can be found in Griffin [50]). *ad hoc* kinematic assumptions used in such beam models introduce errors which become significant blade vibrations are at wavelengths shorter than the length of the blades.

To tackle these issues Prof. Hodges and his collaborators [12, 51] proposed the Generalized Timoshenko Beam Model (GTBM). This technique invloves dimensionally reducing a complex 3-D beam and subsequently solving it as a 1-D beam. The GTBM method, unlike the Timoshenko beam theory, on which it is based, allows for the warping of beam sections once the beam has deformed. The warping is interpolated with the help of a 2-D finite element method and an asymptotic procedure is used to accurately represent, albeit asymptotically, the 3-D strain energy in terms of 6 strain measures of the classical 1-D Timoshenko model (namely the extensional strain, the shear strains and the torsional and bending curvatures). In the 1-D beam representing the blade being analyzed, each section is represented by a 6×6 symmetric stiffness matrix. The stiffness matrix allows the model to capture complex geometry and material properties at that section. This stiffness matrix, along with the 3-D warping functions mentioned earlier can easily be formulated *a priori* and in parallel for all the blade sections used to numerically represent the blade.

The *ad hoc* kinematic assumptions of the classical Timoshenko beam theory are no longer made in the GTBM model. This results in fully populated stiffness matrices

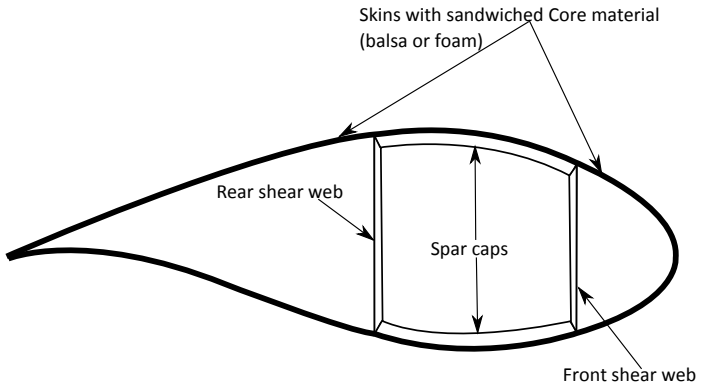

Figure 2.3: Typical internal structure of an airfoil section of a wind turbine blade. The airfoil profile is based on a NACA series airfoil.

ensuring coupling of all 6 modes of deformation. The 1-D beam problem formulated by GTBM, together with the aerodynamic model gives the aeroelastic problem explored in this research. It is an unsteady, non-linear problem advanced in time using an adaptive ODE algorithm. Once the ODE solution is obtained, the warping functions, which had been used to re-formulate the 3-D beam problem as a 1-D nonlinear beam problem, are now used to recover the 3-D fields at each time step of the solution. Figure 2.4 shows how the dynamic and kinematic variables, first represented by an intrinsic coordinate system along the reference line L (beam axis in its original configuration), are transformed into an instantaneous coordinate system along the new configuration l. This explains how the instantaneous position and alignment of each section of the blade is accurately tracked by the intrinsic system.

Figure 2.4 represents the division of the 1-D beam problem into a dynamic and a kinematic part (see Otero and Ponta [29] for a detailed description). The dynamic part is represented by two generalized velocity vectors (linear and angular vibrational

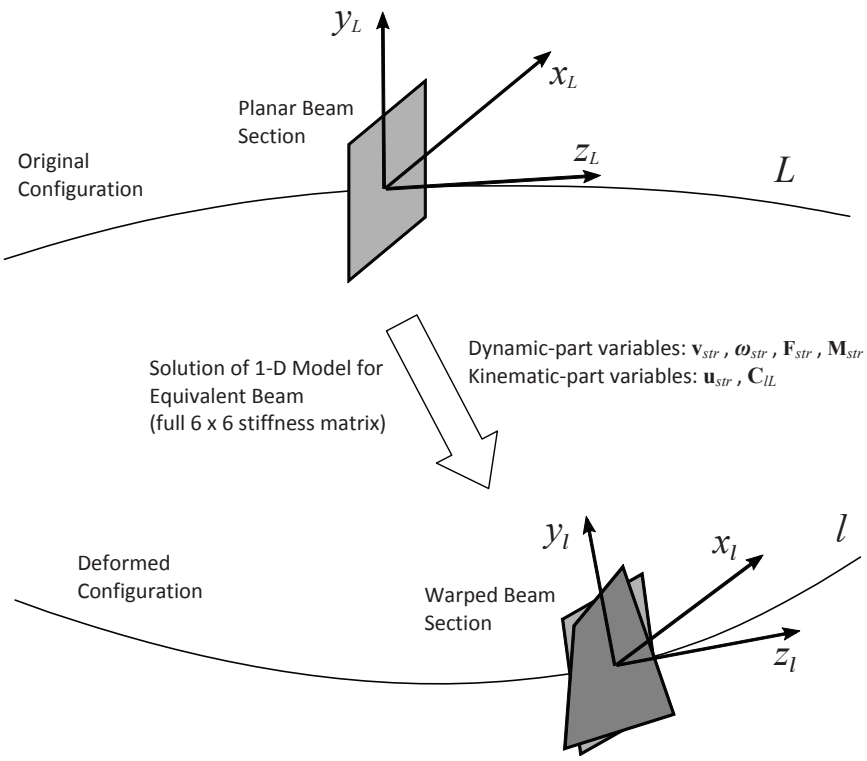

Figure 2.4: A schematic representation of GTBM where the reference line, the beam section and the coordinate system are shown before and after deformation. Also indicated are the variables invloved in the solution's dynamic and kinematic parts.

velocities, $\mathbf{v}_{str}$ and $_{str}$ respectively, of the beam section) and two vectorial components of the generalized forces acting at each section. At every blade section, the 6 components of these force vectors are directly related to the 6 fundamental deformations of the Timoshenko theory through the fully populated 6×6 stiffness matrix mentioned earlier. In order to calculate the linear and angular momentum along with the corresponding forces and moments a 6×6 dimensionally reduced inertia matrix is constructed at every blade section. This sectional inertia matrix accounts for the complicated airfoil shape at that section as well as the sectional material properties and material distribution. It also takes in to account all types of rotational motion

including that of the main shaft or control actions like pitching and yawing. As a result linear and angular acceleration effects, along with the Coriolis and centrifugal forces are all considered. The solution of the dynamic part is further used as an input by the kinematic part to obtain the reference line displacements, $\mathbf{u}_{str}$, along with the orthogonal matrices $\mathbf{C}_{lL}$. These orthogonal matrices are responsible for rotating the blade sections from their original configuration L to the new instantaneous deformed configuration l.

The displacements $\mathbf{u}_{str}$, the linear and angular vibrational velocities of each blade section and the $\mathbf{C}_{lL}$ matrices are updated at every time-step of the ODE solution of the structural model. These updated variables are key to the feedback between the structural and aerodynamic models. It should be pointed out that the flow of information from the aerodynamic to the structural side is in terms of forces acting on blade sections resulting from aerodynamic loads. These are distributed forces resulting from lift, drag and aerodynamic pitching moment on the airfoil sections.

These numerical schemes work as part of a multi-physics ODE solver called the Common Ordinary Differential Equation Framework (CODEF) [8].In addition to the aeroelastic model (CODEF)incorporates several modules to include the effects of control system dynamics and also of electromechanical devices on the drive-train. Such an integral multi-physics modeling tool using an ODE solution in time could include other aspects that affect rotor dynamics, simply by adding another module to the

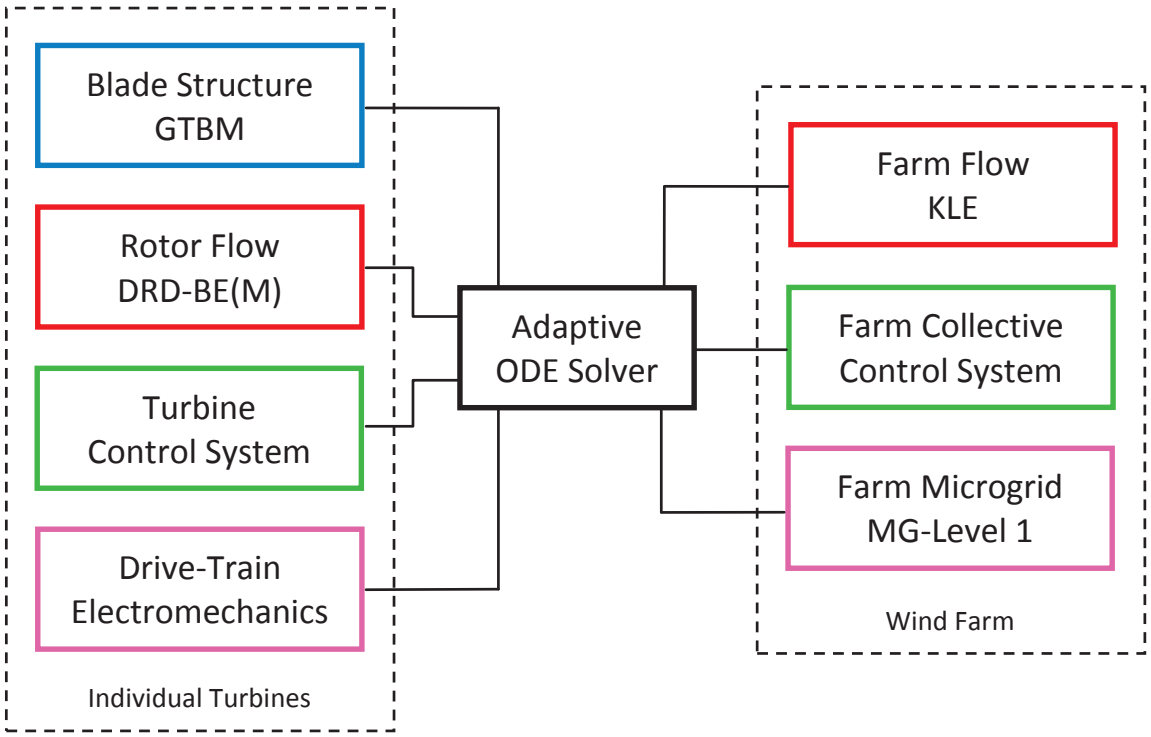

Figure 2.5: Flow-chart diagram of the Common ODE Framework.

flexible (CODEF) framework.

2.3 The common ODE framework (CODEF)

As explained in the previous paragraph, the 1-D beam problem is solved using a nonlinear adaptive ODE solver. The ODE solver is essentially a variable-timestep/variable-order algorithm which by monitoring the local truncation error at each timestep, improves the efficiency and stability of the time marching numerical scheme. As mentioned earlier, the control system dynamics and electromechanical device dynamics can be added to the (CODEF) simply as new modules consisting of the

differential equations representing their dynamic behaviour. This way more components to the feedback system already present in the aeroelastic model can be addded in the form of modifications to the boundary conditions of each component/module of the (CODEF). A nonlinear adaptive ODE algorithm as a *common framework* is, therefore, ideal for integrating all the dynamic components of a wind turbine rotor. Figure 2.5 shows a flow-chart diagram of the global (CODEF) outlining the interrelations between different modules. These modules may each be explored and worked on individually, thereby, simplifying further development of the code by the improvement and/or expansion of each individual module independently. The (CODEF), thus, allows for the addition of innovative control strategies along with all physical aspects of wind turbine dynamics (electrical or mechanical) to the aeroelastic analysis using a self adaptive ODE algorithm. This modular approach is perfectly suited for interconnecting the dynamics of an individual turbine into a model that simulates the dynamics of a wind-farm, including not just turbine-to-turbine aerodynamic interaction but also electrical, and collective control of the entire farm.

Before getting into the DRD-BEM procedure it is important to first understand the standard BEM model in detail.

2.4 Blade Element Momentum Model

As mentioned in the introduction to this chapter there are two major distinct approaches to modeling a HAWT - the stream-tube approach and the vortex modeling approach. In the vortex modelling approach the blades along with their wakes are replaced by their vortex representations and the flow across the turbine as well as in the wake is solved as a potential flow problem. The Stream-Tube approach involves performing a momentum balance across one or more stream-tubes enclosing the rotor area. The Blade Element Momentum (BEM) model is the most widely used modeling approach for HAWTs, and as mentioned in the introduction, that is what this dissertation focuses on. In this chapter the theoretical basis of BEM is elaborated upon followed by a detailed explanation of the DRD-BEM algorithm.

The Blade Element Momentum theory, also called BEM, proposed almost a century ago [4, 42], is still the preferred aerodynamic component for analyzing wind turbines. There have been several improvements and corrections to the classical BEM technique but the basic theory still remains the same. BEM has its origins in the blade element and the momentum theories. In the momentum theory the change in momentum across an annular stream tube of the rotor is essentially attributed to the aerodynamic lift and drag forces acting on the blade element at that annular region. These forces are obtained by the blade element theory, and hence the name Blade Element

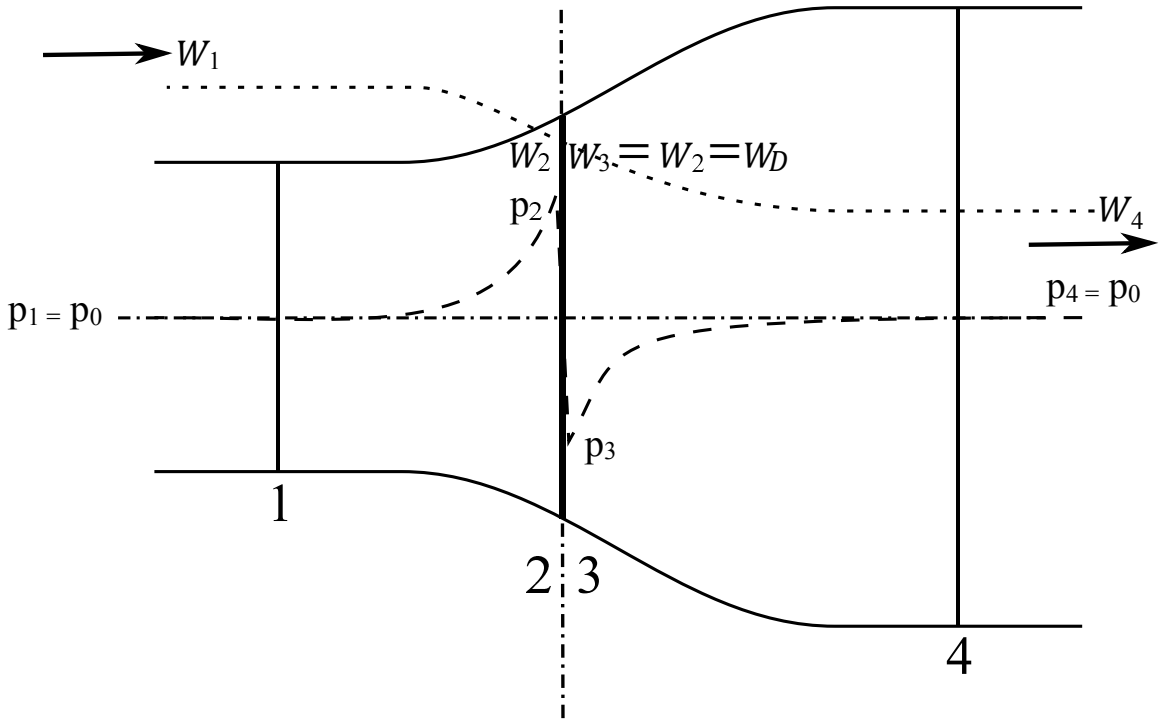

Figure 2.6: Schematic representation of the pressure and velocity drop across a 1-D Actuator Disk model and the corresponding wake expansion.

Momentum theory. The next two sections tackle each component of the BEM theory individually before bringing them together to form the Blade Element Momentum model.

2.4.1 The 1-D Actuator Disk theory

The momentum theory finds it origins in the axial momentum theory as an actuator disk model first proposed by Rankine [52] and elaborated upon by W. Froude [53] and R.E. Froude [54]. In its simplest form an actuator disk model consists of a circular

actuator disk replacing the wind turbine. As seen in figure 2.6, as the wind flows across the disk, it is gradually slowed down by the actuator disk while there is a discontinuous drop in pressure across it. Assuming only axial flow, with no rotational component there are two ways to find the thrust acting on the disk as a result of the flow. The drop in velocity from far upstream to far downstream (i.e. between regions 1 and 4 in figure 2.6) can be used to find the change in momentum due to the thrust T exerted by the disk on the wind.

$$T = \dot{m}(W_1 - W_4) = \rho\, A\, W_D(W_1 - W_4) \tag{2.1}$$

Where, ρ is the density of air and A is the area of the actuator disk

On the other hand the pressure difference across the disk results in a thrust given by

$$T = A(p_2 - p_3) \tag{2.2}$$

On applying the Bernoulli equation between regions 1 and 2 and again between regions 3 and 4 (and therefore not including the disk) equation 2.2 can be written as

$$T = 0.5\, \rho\, A({W_1}^2 - {W_4}^2) \tag{2.3}$$

Equations 2.2 and 2.3 give

$$W_D = 0.5(W_1 + W_4) \tag{2.4}$$

An axial induction factor a can be defined at this point in order to quantify the influence of the disk on the wind as:

$$W_1 - W_2 = a\, W_1 \tag{2.5}$$

Then by equation 2.4

$$W_1 - W_4 = 2\, a\, W_1 \tag{2.6}$$

This when introduced into equation 2.3 for thrust gives

$$T = 2\, \rho\, A\, {W_1}^2 (1 - a) \tag{2.7}$$

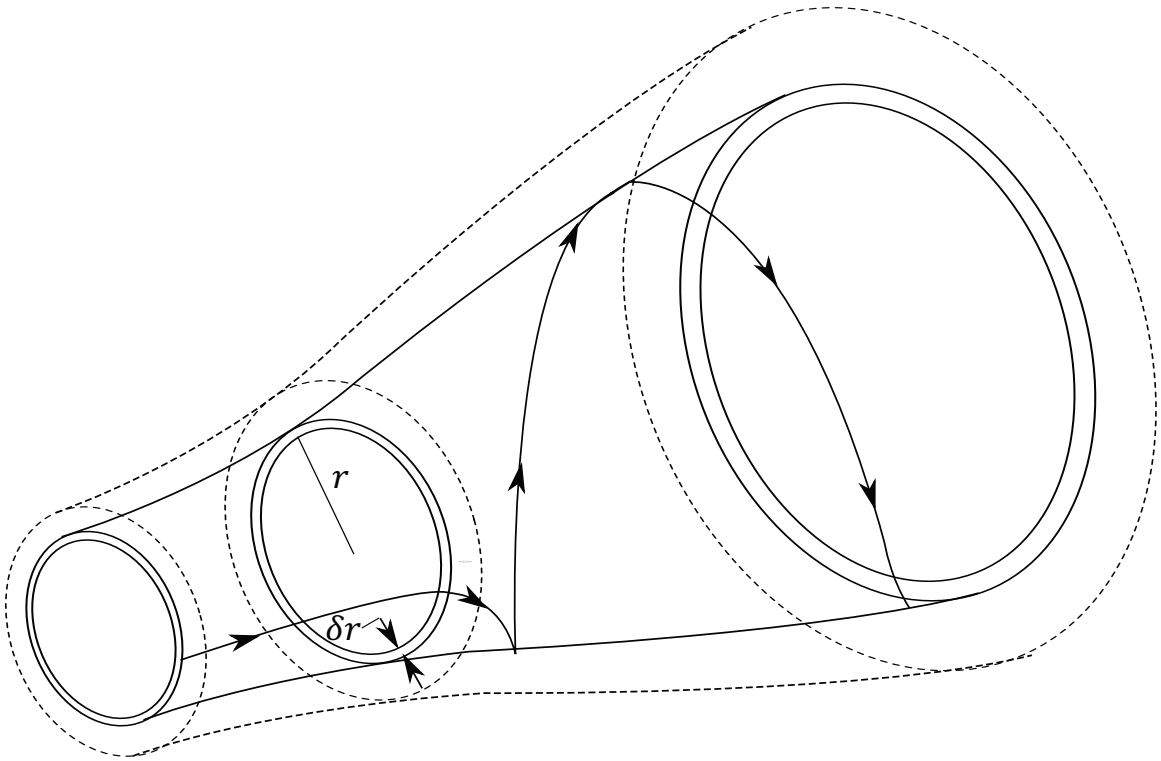

Figure 2.7: Annular stream-tube model with rotation of flow behind rotor.

2.4.2 The General Momentum Theory

For the general momentum theory an annular stream-tube model of the actuator disk is used. Figure 2.7 shows an annular stream-tube of thickness δr at a distance r from the center of the actuator disk. Unlike the axial momentum theory, here the rotational motion in the slipstream is included. Let Ω be the angular velocity of the turbine and ω be the angular velocity imparted to the wind as it flows across the turbine. Therefore, the angular velocity of flow relative to the turbine blades increases to $(\Omega + \omega)$ downstream of the turbine. Applying Bernoulli's equation to the

flow relative to the moving turbine blades the increase in pressure across the disk is given by:

$$p_2 - p_3 = \rho(\Omega + \frac{1}{2}\,\omega)r^2\omega \tag{2.8}$$

The thrust and torques as a result of this additional rotational component are given by:

$$\delta T = \delta A(p_2 - p_3) = 2\,\pi\,r\,\delta r[\rho(\Omega + \frac{1}{2}\,\omega)r^2\omega] \tag{2.9}$$

$$\delta Q = \dot{m}_{strip}\,r^2\omega = 2\,\pi\,r\,\delta r\,r^2\omega\,\rho\,W_2 \tag{2.10}$$

Where, δA represents the area of the annular region and $\dot{m}_{strip}$ is the mass flow rate through the annular strip.

Assuming that the tangential velocity induced at the rotor plane is given by $\Omega\,r\,a'$ and that induced velocity downstream of the rotor is given by $2\,\Omega\,r\,a'$ where a' is the tangential induction factor representing the increase in relative tangential velocity in the blades cross-section due to wake rotation and is given by

$$a' = \Omega / 2\,\pi \tag{2.11}$$

The expression for the thrust can now be written as

$$\delta T = 4\,\pi\,r\,\delta r\,r^2\,\rho\,\Omega^2(1+a')a' \tag{2.12}$$

A careful examination of this expression for thrust reveals that it has a component of pressure drop added to it in excess of the static pressure drop seen in equation ref in the axial momentum theory. This drop in pressure given by:

$$\Delta p = 2\,\rho\,r^2\,\Omega^2\,a'^2 \tag{2.13}$$

accounts for the kinetic energy of the rotating fluid and will later be used as an added term in the axial momentum balance [2].

2.4.3 Blade Element Theory

The thrust and torque in the general momentum theory was calculated for an annular strip in the actuator disk representing the turbine rotor. The blade element theory

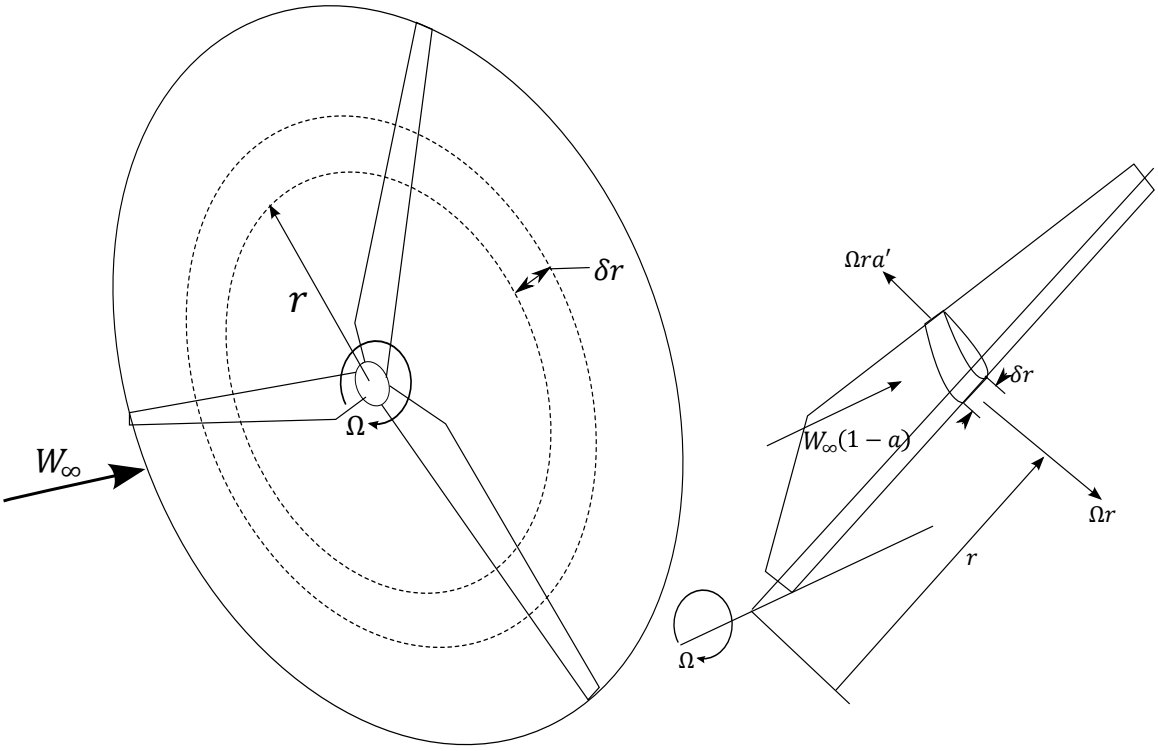

Figure 2.8: The annular ring swept out by the blade element element shown on the figure of the blade on the right at distance r from the hub as it rotates at an angular velocity Ω.

aims at finding the forces acting on a blade element of the rotor at that radius (r in the case explained in the previous section) with thickness δr. This is done by assuming that the aerodynamic forces acting on a blade element can be described by using the 2-D airfoil characteristics of the airfoil profile at that section. This is schematically explained in figure 2.8. These characteristics are obtained based on the angle of attack resulting from the resultant velocity of incident wind at that section. From figure ref it can be seen that the relative velocity at the blade section is given by:

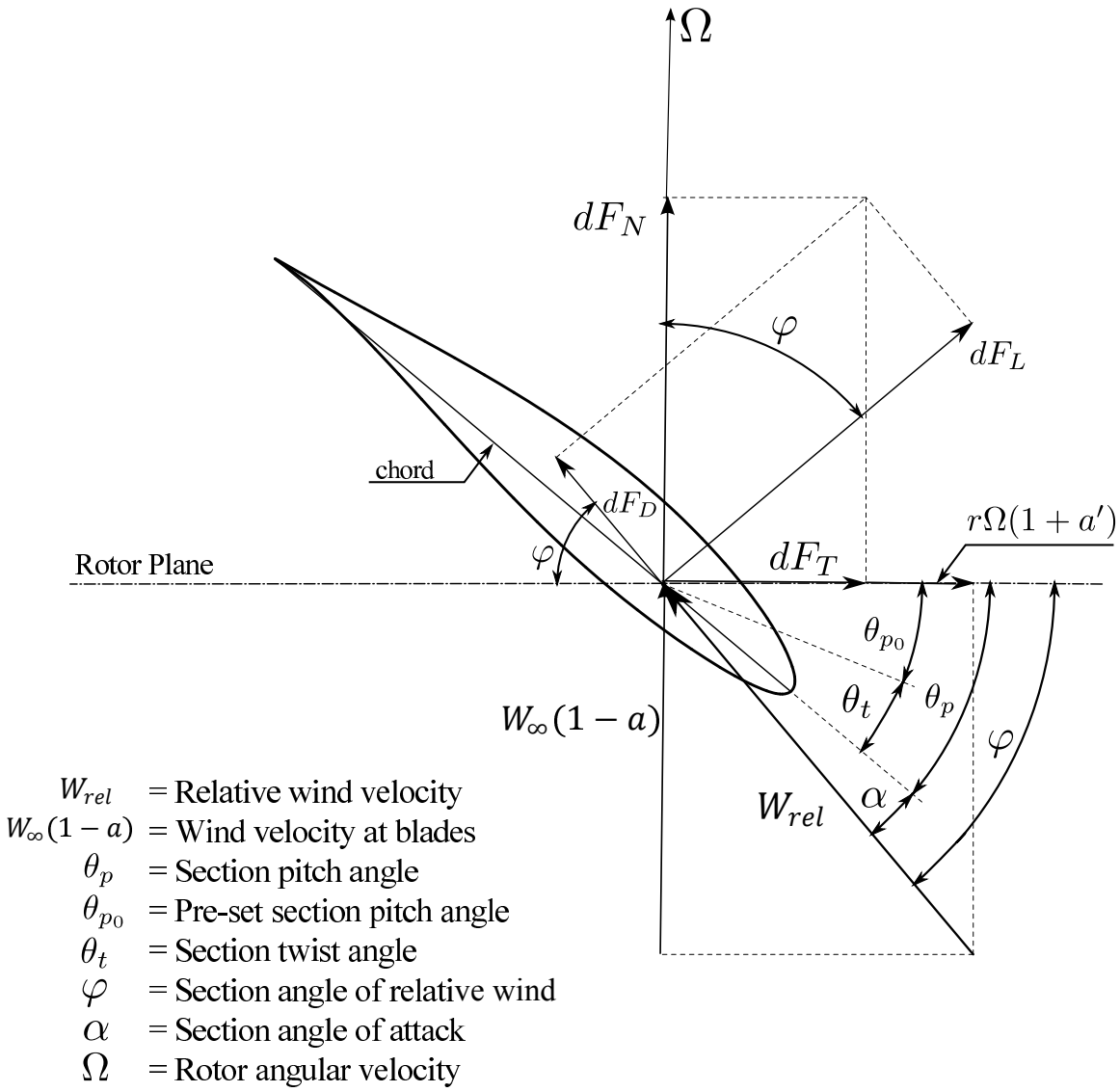

Figure 2.9: Velocities, forces and definitions of relevant angles on a blade element.

$$W_{rel} = \sqrt{(W_\infty(1-a))^2 + (\Omega\, r(1+a'))^2}, \tag{2.14}$$

And the angle of incidence ϕ of this velocity is given by: $sin\,\phi = [W_\infty(1-a)]/W_{rel}$ and $cos\,\phi = [r\,\Omega(1+a')]/W_{rel}$

The angle θ_p (the section pitch angle) together with the angle of relative wind ϕ give the angle of attack α as:

$$\alpha = \phi - \theta_p \tag{2.15}$$

using this α the lift and drag coefficients C_l and C_d at the blade section can be obtained from the aerodynamic data for the airfoil profile at that section. The lift force δF_L normal to the relative wind velocity and the drag δF_D acting along the relative wind are obtained from these coefficients by the following relations:

$$\delta F_L = \frac{1}{2}\rho\, c {W_{rel}}^2 C_l\, \delta r \tag{2.16}$$

$$\delta F_D = \frac{1}{2}\rho\, c {W_{rel}}^2 C_d\, \delta r \tag{2.17}$$

Where ρ is the air density, c is chord length and δr is the spanwise thickness of the blade element.

Based on these forces the total axial thrust δT and the torque δQ on the annular ring at a radius r for a turbine with B number of blades is given by:

$$\delta T = \delta L\, cos\phi + \delta D\, sin\phi = \frac{1}{2}\rho\, c\, B {W_{rel}}^2 (C_l\, cos\phi + C_d\, sin\phi)\delta r \tag{2.18}$$

$$\delta Q = (\delta L\, sin\phi - \delta D\, cos\phi)r = \frac{1}{2}\rho\, c\, B{W_{rel}}^2(C_l\, sin\phi - C_d\, cos\phi)r\, \delta r \tag{2.19}$$

2.4.4 Blade Element Momentum Theory

As explained in the introduction to this chapter, in the Blade Element Momentum (BEM) Theory rate of change in momentum across the annular sections of the rotor is equated to the forces acting on that section as obtained by the blade element theory explained above. As long the distribution of circulation over the blade is fairly uniform ensuring a concentration of vortices shed mostly at the root and the tips [40], the general momentum theory explained above works with the assumption that each annular strip can be analyzed independently. Also, as the wake behind the turbine expands the interaction between the vortices shed is somewhat negated and therefore, this assumption works better for turbines than for propellers [40]. As far as the blade element theory is concerned spanwise flow is ignored and the airfoil data obtained from 2-D airfoil tests are used. This assumption gains importance when the blade is no longer perpendicular to the axis of rotation and forms the crux of this dissertation as will be elaborated upon in subsequent chapters. The basis of BEM is to relate the local induction factors of axial and tangential velocities to the coefficient of thrust at that rotor section. And this is done by essentially performing a momentum balance in the axial and tangential directions at all of the annular stream-tube that together

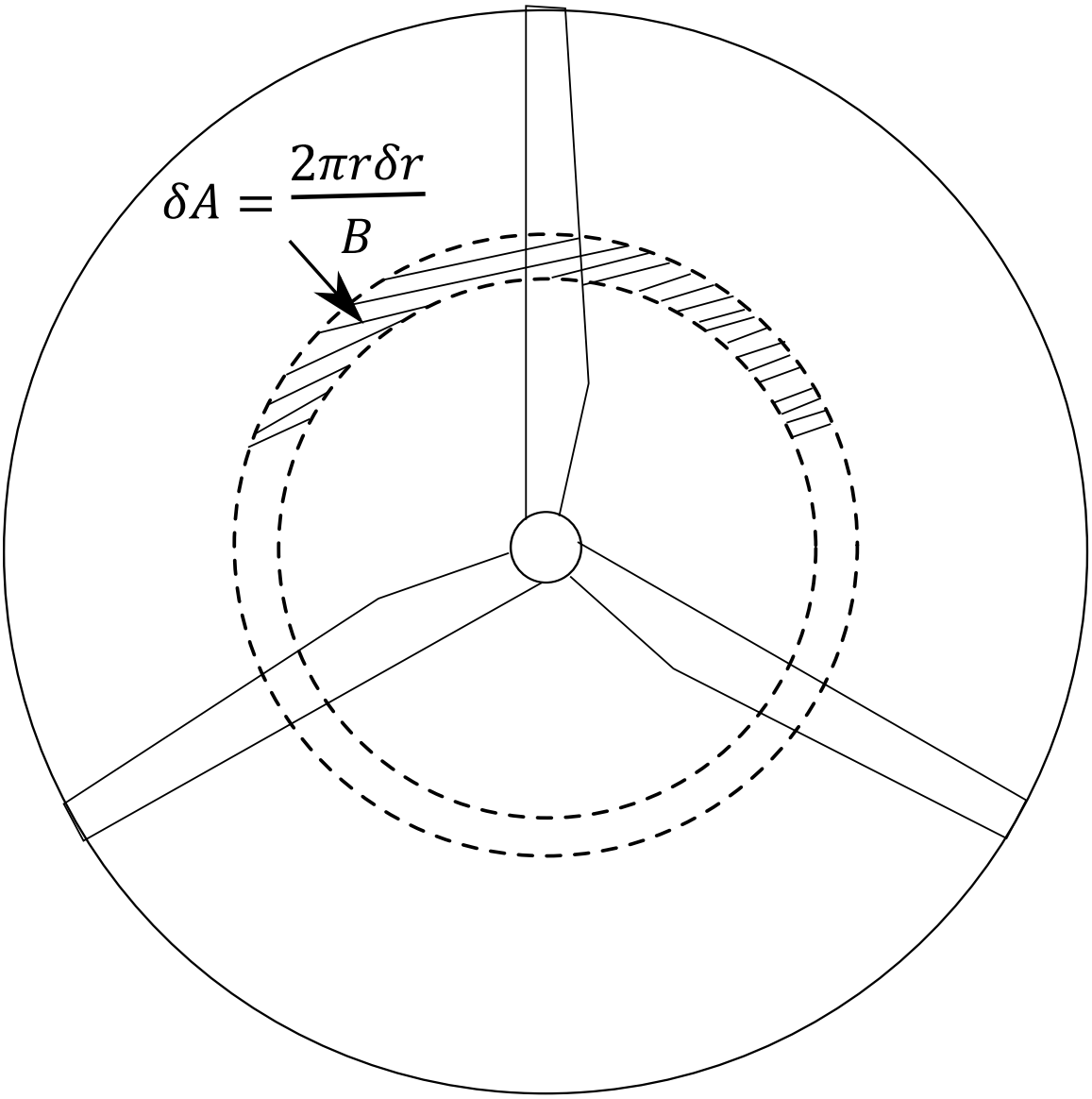

Figure 2.10: The annular strip on which the effect of forces at the blade element are assumed to have an affect for BEM analysis.

comprise the rotor disk. Looking at figure 2.10, if blade 1 is to analyzed the force acting on this blade at that section is assumed to have an affect on the wind flowing across the entire shaded region [55].

Using equation 2.7 the axial thrust on this shaded region can be used to define the rate

of change of axial momentum with area of the annular strip given by $\delta A = 2\,\pi\,r\,\delta r$ for a turbine with B number of blades.

$$\delta T = \frac{2\,\pi\,r\,\delta r}{B}\,\rho\,{W_\infty}^2\,2a(1-a) \tag{2.20}$$

However, as mentioned in section 2.4.2 equation 2.13, the additional drop in static pressure must be accounted for and that is done by adding the following axial force on the annulus based on the explanation found in [2] $0.5\,\rho(2\,a'\,\Omega\,r)^2\,2\,\pi\,r\,\delta r$. This gives the new equation for the rate of change of axial momentum as

$$\delta T = \frac{4\,\pi\,r\,\delta r}{B}\,\rho\,({W_\infty}^2\,a(1-a) + (a'\,\Omega\,r)^2) \tag{2.21}$$

Similarly the rate of change of tangential momentum can be defined by the torque acting on that annular strip as:

$$\delta Q = \frac{4\,\pi\,r^2\,\delta r}{B}\,\rho\,W_\infty\,(1-a)r\,\Omega\,a' \tag{2.22}$$

Going back to figure 2.8, the figure on the right represents blade 1 and the airfoil at radius r has been drawn as a section within the blade for clarity. The forces acting

on this blade element have been shown in detail in figure 2.9. Therefore using the equations 2.18 and 2.19, the thrust and torque from the blade element theory can be equated to the rate of change in axial and tangential momentum of equations 2.21 and 2.22 to give

$$\frac{1}{2}\rho\, c\, {W_{rel}}^2 (C_l\, cos\phi + C_d\, sin\phi)\delta r = \frac{4\,\pi\, r\, \delta r}{B}\,\rho\,({W_\infty}^2\, a(1-a) + (a'\,\Omega\, r)^2) \tag{2.23}$$

$$\frac{1}{2}\rho\, c\, {W_{rel}}^2 (C_l\, sin\phi - C_d\, cos\phi) r\, \delta r = \frac{4\,\pi\, r^2\, \delta r}{B}\,\rho\, W_\infty\,(1-a) r\,\Omega\, a' \tag{2.24}$$

As mentioned earlier in this section, these equations are iteratively solved to relate the local thrust coefficient to the local induction factors. The iterative procedure used in this research builds on the Dynamic Rotor Deformation - BEM or the DRD-BEM method which will be described in the following section. There are a number of corrections applied to this procedure to account for the various assumptions mentioned earlier. These corrections will be explained in the context of the DRD-BEM procedure

The following sections provide a detailed explanation of the standard DRD-BEM model, thereby, providing the necessary context to the crux of this dissertation.

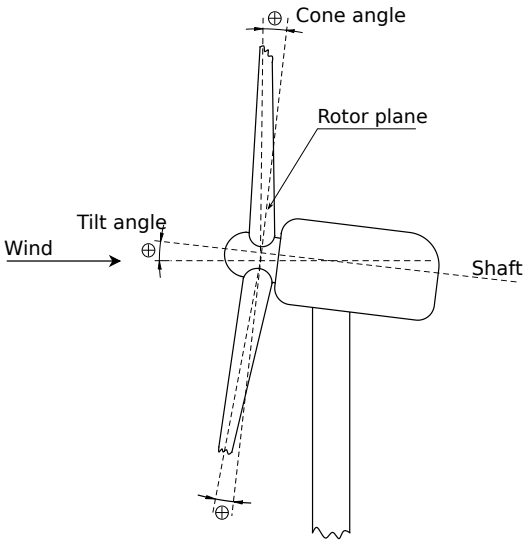

Figure 2.11: Cone angle θ_{cn} and tilt angle θ_{tlt} for upwind turbines, as given by the International Electrotechnical Commission (IEC) standards [3]

2.4.5 DRD-BEM procedure

The algorithmic sequence followed by the DRD-BEM model is as follows:

2.4.5.1 Applying the induction factor on the undisturbed wind

Velocity vector, $\mathbf{W}_h$, through an annular actuator in the hub coordinate system h can be written as,

$$\mathbf{W}_h = \begin{bmatrix} W_{\infty h_x}(1-a) \\ W_{\infty h_y} + \Omega\, r_h a' \\ W_{\infty h_z} \end{bmatrix}, \tag{2.25}$$

where a is the axial induction factor representing the deficit in wind velocity in the axial direction and a' is the tangential induction factor representing an increase in the tangential component of wind velocity as flows across the actuator. $\mathbf{W}_{\infty h}$ is the undisturbed wind velocity in the h (hub) coordinate system (figure 2.2), Ω is the angular velocity of the rotor, and r_h is the instantaneous radial distance of a section of the blade from the hub in the h (hub) coordinate system (see figure 2.1). This three dimensional representation of $\mathbf{W}_h$ shows how an annular stream-tube corresponding to a certain blade element gets deflected by the forces exerted on it by the associated annular actuator. Misalignments like tilt, yaw, changes in wind direction etc. are also taken into account by orthogonal matrices which effectively transform the undisturbed incoming velocity represented in the wind coordinate system into $\mathbf{W}_{\infty h}$. The first of the set of orthogonal matrices acting on $\mathbf{W}_{\infty wind}$ is $\mathbf{C}_{\Delta\theta_{yaw}}$ which takes into account misalignments between wind direction and nacelle orientation representing a rotation around the vertical axis.

$$\mathbf{C}_{\Delta\theta_{yaw}} = \begin{bmatrix} \cos(-\Delta\theta_{yaw}) & \sin(-\Delta\theta_{yaw}) & 0 \\ -\sin(-\Delta\theta_{yaw}) & \cos(-\Delta\theta_{yaw}) & 0 \\ 0 & 0 & 1 \end{bmatrix}, \tag{2.26}$$

where $\Delta\theta_{yaw} = \theta_{yaw} - \theta_{\infty}$, with the nacelle orientation given by θ_{yaw} and the undisturbed wind direction is given by θ_{∞}. The negative sign is because $\Delta\theta_{yaw}$ is defined positive counter-clockwise according to (TS 61400-13 EIC:2001), and θ_{yaw} as well as

θ_∞ are defined positive clockwise from the North as in a compass rose. The misalignment in the vertical direction brought about by tilt as defined by IEC standards [3] is accounted for by $\mathbf{C}_{\theta_{tlt}}$ (figure 2.11). Finally, the orthogonal matrix $\mathbf{C}_{\theta_{az}}$ rotates the blade around the main shaft to bring it to its new instantaneous azimuthal position, thereby, transforming the wind velocity into the *hub* coordinate system h. Thus, the undisturbed wind velocity in the hub coordinate system is given by:

$$\mathbf{W}_{\infty h} = \left(\mathbf{C}_{\theta_{az}}\mathbf{C}_{\theta_{tlt}}\mathbf{C}_{\Delta\theta_{yaw}}\mathbf{W}_{\infty wind}\right). \tag{2.27}$$

2.4.5.2 projecting the Velocity vector so obtained onto the instantaneous coordinate system of the deformed blade section

$\mathbf{W}_h$ obtained in the previous step is projected on to the coordinate system of deformed blade section through more coordinate transformations. First is the transformation matrix $\mathbf{C}_{\theta_{cn}}$ which takes into account rotor coning (see figure 2.11).

This could be a fixed angle for a pre-coned rotor or as a control mechanism which changes the coning angle by using a variable matrix reflecting said action instantaneuosly. A detailed description of the concept of coning rotors is given in Jamieson [17], Crawford and Platts [18], Crawford [22]. Next is the pitching transformation matrix $\mathbf{C}_{\theta_p}$ which represents a rotation around the blade's pitching axis i.e. the third

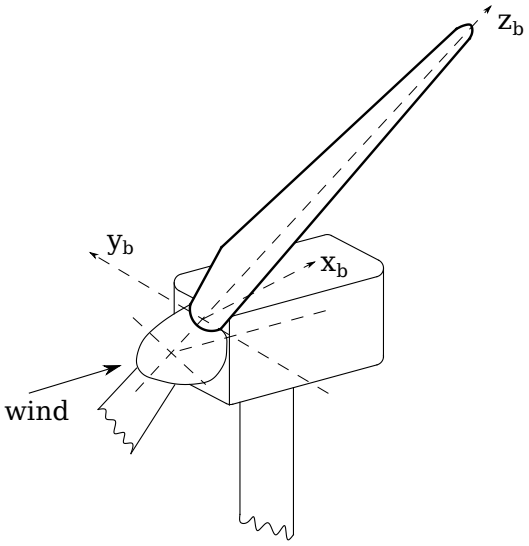

Figure 2.12: The Blade coordinate system as defined by the International Electrotechnical Commission (IEC) standards [3]

axis of the coordinate system obtained in the previous step which accounted for coning . This gives the *blade* coordinate system. The *blade* coordinate system is represented by the subscript b as per IEC standards [3] (see figure 2.12).

$$\mathbf{C}_{\theta_\mathbf{p}} = \begin{bmatrix} \cos(-\theta_p) & \sin(-\theta_p) & 0 \\ -\sin(-\theta_p) & \cos(-\theta_p) & 0 \\ 0 & 0 & 1 \end{bmatrix}, \tag{2.28}$$

Here the pitch angle $\theta_p = \theta_{p_0} + \theta_{p_{ctrl}}$, where, θ_{p_0} is hte pre-set fixed pitch, while $\theta_{p_{ctrl}}$ can be varied by the control system. The negative sign is for the sense in which the positive pitch angles are defined in IEC standards. This Combination of a fixed angle

with a changing control angle can also be applied to $\mathbf{C}_{\theta_{tlt}}$ in case tilting is used as a control mechanism. As mentioned in the explanation for CODEF, the DRD-BEM can interact with control modules, hence, the projection matrices for these actions must be updated at every instant of the solution. As an example, $\mathbf{C}_{\theta_{az}}$, will not only compute instantaneous blade position, but also reflect control actions which can affect the angular speed Ω of the rotor.

The beam axis in its original configuration is represented by the reference line, L, and is not always aligned with the third axis of coordinate system b shown in figure 2.12. This is because of the possiblity of pre-conformed curvatures introduced during blade manufacture as part of blade design. The orthogonal matrix $\mathbf{C}_{Lb}$, computed along L, at each location of analysis, relates the b coordinate system, with the intrinsic coordinate system of the the non-deformed blade section configuration (x_L, y_L, z_L) defined along L. Finally, the orthogonal matrix $\mathbf{C}_{lL}$ is provided by the solution of the kinematic equations on the structural model (as explained in section 2.2). This matrix transforms all necessary vectors from L coordinate system to the deformed blade section coordinate system l.

After projecting the velocity vector $\mathbf{W}_h$ onto the blade section coordinate system, $\mathbf{v}_{str}$ and $\mathbf{v}_{mech}$ are added to it. $\mathbf{v}_{str}$ is the vibrational velocities at the blade section as obtained by the structural model while $\mathbf{v}_{mech}$ are the velocities associated with the combined action of mechanical devices (like yaw, pitch, and azimuthal rotation) on

the blade section. Thus, the velocity of relative wind, $\mathbf{W}_l$, at the blade section is:

$$\mathbf{W}_l = \left(\mathbf{C}_{lL}\mathbf{C}_{Lb}\mathbf{C}_{\theta_p}\mathbf{C}_{\theta_{cn}}\mathbf{W}_h\right) + \mathbf{v}_{str} + \mathbf{v}_{mech}. \tag{2.29}$$

2.4.5.3 Using the Blade Element Theory to obtain the aerodyanmic forces on the blade section

Using the magnitude of the relative wind velocity in the plane of the blade section, $W_{rel} = \sqrt{{W_{l_x}}^2 + {W_{l_y}}^2}$, and the corresponding angle of attack α, the associated lift and drag forces per unit length of span can be estimated by:

$$dF_{lift} = \frac{1}{2}\rho\, C_l\, W_{rel}^2\, c\,, \qquad dF_{drag} = \frac{1}{2}\rho\, C_d\, W_{rel}^2\, c, \tag{2.30}$$

where C_l and C_d represent the lift and drag coefficients for the corresponding angle of attack, ρ stands for air density, and c is the chord length of the airfoil at that blade section. The net aerodynamic load acting on the blade element of span δl (figure 2.1) aligned with the relative wind is given by

$$\delta\mathbf{F}_{rel} = \begin{bmatrix} dF_{lift} \\ dF_{drag} \\ 0 \end{bmatrix} \delta l, \tag{2.31}$$

2.4.5.4 Projecting the aerodynamic forces back onto the hub coordinate system

The force vector $\delta\mathbf{F}_{rel}$ is projected back onto the h coordinate system by

$$\mathbf{F}_h = \mathbf{C}_{\theta_{cn}}^T \mathbf{C}_{\theta_p}^T \mathbf{C}_{Lb}^T \mathbf{C}_{lL}^T \mathbf{C}_{Lthal}\, \mathbf{dF}_{rel}\, \delta l, \tag{2.32}$$

where $\mathbf{C}_{Lthal}$ projects the lift and drag from the Lilenthal system onto the l coordinate system (aligned with the chord-normal and chord-wise directions of the airfoil). The above expression can also be written as $\mathbf{F}_h = \mathbf{dF}_h\, \delta l$, or as

$$\mathbf{F}_h = \begin{bmatrix} \delta F_{h_x} \\ \delta F_{h_y} \\ \delta F_{h_z} \end{bmatrix} = \begin{bmatrix} dF_{h_x} \\ dF_{h_y} \\ dF_{h_z} \end{bmatrix} \delta l, \tag{2.33}$$

where $\mathbf{dF}_h = \mathbf{C}_{\theta_{cn}}^T \mathbf{C}_{\theta_p}^T \mathbf{C}_{Lb}^T \mathbf{C}_{lL}^T \mathbf{C}_{Lthal}\, \mathbf{dF}_{rel}$.

2.4.5.5 Equating the forces from Blade Element Theory to those obtained by the Momentum Theory

Components of force vector $\mathbf{F}_h$ are equated to the rate of change of momentum of the wind as it flows across the corresponding annular actuator. First, the axial component δF_{h_x}, normal to the axis of the annular actuator, is equated to the rate of change in momentum of $W_{\infty h_x}$ corresponding to the axial interference factor a (see expression 2.25), giving

$$dF_{h_x} = f_{th} \frac{4\pi\,\rho\,r_h}{B} \left(W_{\infty h_x}^2\, a\,(1-a) + (a'\Omega\,r_h)^2 \right) \frac{\delta r_h}{\delta l}, \tag{2.34}$$

where f_{th} represents the tip and hub loss factors explained in some detail in section 2.4.6, and B represents the number of blades. The term $(a'\Omega\,r_h)^2$, as explained in detail in the dscussion on BEM theory, is added to account for pressure drop behind the actuator. $\frac{\delta r_h}{\delta l}$ is added to transform δl into δr_h using the same orthogonal matrices as earlier. In the same fashion, δF_{h_y}, is equated to the rate of change in momentum associated with the tangential induction factor a' as

$$dF_{h_y} = f_{th}\, \frac{4\pi\,\rho\,r_h}{B}\, |W_{\infty h_x}|\,(1-a)\,(\Omega\,r_h)\,a'\,\frac{\delta r_h}{\delta l}. \tag{2.35}$$

2.4.5.6 Using an iterative minimization algorithm to solve for the induction factors

Equations (2.34) and (2.35) form a nonlinear system of equations where both a and a' are unknown. In classical BEM, this is solved by functional iteration schemes which start at an initial guess value for each blade element. However, since DRD-BEM is a more complex model, it uses an advanced optimization algorithm making the iterative process faster and more stable.First a set of implicit expressions for a and a' are derived as:

$$a_{Res} = dF_{h_x} - f_{th}\frac{4\pi\,\rho\,r_h}{B}\left(W^2_{\infty h_x}\,a\,(1-a) + (a'\Omega\,r_h)^2\right)\frac{\delta r_h}{\delta l}, \tag{2.36}$$

$$a' = \frac{dF_{h_y}\,B}{f_{th}\,4\pi\,\rho\,r_h\,|W_{\infty h_x}|\,(1-a)\,(\Omega\,r_h)\,\frac{\delta r_h}{\delta l}} \tag{2.37}$$

A minimization of a_{Res} in equation (2.36) is done to obtain the axial induction factor a, using an updated value of a' from expression (2.37) at each iteration acting as a constraint. The minimization process consists of an advanced adaptive algorithm using a combination of bisection, secant, and inverse quadratic interpolation. This ensures bracketing the search within an expected range. This helps avoid solution overshoots, divergence or the possibility of getting trapped in infinite loops.

2.4.5.7 Computation of the distributed aerodynamic loads

Once the the induction factors are computed, the aerodynamic forces can be calculated by repeating steps 2.4.5.1 to 2.4.5.3, but then projecting the forces obtained in 2.4.5.3 onto the l coordinate system. This is done as follows

$$\mathbf{dF}_l = \mathbf{C}_{Lthal}\, \mathbf{dF}_{rel} \tag{2.38}$$

The first two components of $\mathbf{dF}_l$ represent the aerodynamic loads in the chord-normal and chord-wise directions. The aerodynamic moment per unit length of the span on that airfoil section around the first axis of l, is given by

$$dM_{aer} = \frac{1}{2}\rho\, C_m\, W_{rel}^2\, c^2 \tag{2.39}$$

C_m represents the aerodynamic pitch coefficient of the airfoil for the angle of attack at that section. These sectional aerodynamic loads are assembled to give the distributed loads on the blade. The effect of gravitational loads on the distributed forces and moments is also taken into account for the instantaneous position and attitude of each blade section. This is done using the inertia properties obtained from the dimensionally-reduced inertia matrix contructed for the equivalent beam as explained in section 2.2. These forces act as the input for the GTBM structural model (see section 2.2).

2.4.6 Dynamically updating the corrective factors used in BEM models

Unlike classical BEM where the corrective factors were computed at the begining and then kept constant throughout the calculation, in DRD-BEM they are updated at every iteration:

† Aerodynamic data for each of the airfoils as obtained from static wind-tunnel tests are dynamically corrected to include rotational-augmentation (based on models of Du and Selig [56] and Eggers [57]) and dynamic-stall (based on the works of G. and S. [48], Leishman et al. [58] and Leishman and Beddoes [59]) effects.

† Multiple data tables , each consisting of aerodynamic coefficients of different airfoils. Each set of data can be associated with various factors effecting aerodynamic properties of airfoil from varying Reynolds number to adding flow control devices . The exact values of aerodynamic properties can then be interpolated from the appropriate table and accordingly updated.

† The Vieterna extrapolation was proposed by Viterna and Janetzke [60] to extend the aerodynamic data availability for a wide range of angles of attack $\pm 180°$.

The following empirical corrections typically seen in most current implementations of BEM models ([see 2, 43]), have also been included in DRD-BEM:

† The tip-loss and hub-loss factor f_{th} in equations (2.34) to (2.37) correcting the induced velocity due to vortex shedding from the tip and root of each blade, not accounted for by BEM theory.

To account for the difference in flow dynamics between an actuator disk representing essentially an infinitely bladed rotor and an actual turbine with finite number of blades, Prandtl introduced the tip-loss factor. With a finite number of blades, the circulation around the blade has to decrease continuously to zero towards the tip, because of the possibility of a cross-flow around the tip, which decreases the pressure difference between upper and lower side of the tip profile. This effect is analogous to that of an airplane wing of finite span, but the vortex calculations are more complex in case of a wind turbine. The model must include the effect of interaction of vortices shed by rotor blades with the flow. The most basic definition of tip losses is given as the ratio of circulation of Γ_B for a rotor with B blades to the circulation for an infinitely bladed rotor disk given by Γ_∞ The DRD-BEM algorithm included a factor f_{th} to account for these interactions which have a significant influence on the thrust and torque output of the rotor. The factor used in DRD-BEM accounts for both tip and hub losses since vortices are also shed at the root of the blade and their interaction with

the wake must also be accounted for.

Prandtl [61] estimated this "tip-loss" effect for a lightly loaded rotor with negligible wake expansion. He considered the helical vortex sheets behind the turbine to be rigid planes moving with a velocity equal to the axial induced velocity aW_∞ with respect to the undisturbed external flow. He simplified this by considering these 'flat plates' to be equidistant. He then went on to solve it as a potential flow problem of flow around semi-infinite plates. A conformal mapping was used to solve this problem and find the reduction in potential difference between two plates approaching the tip. This reduction was assumed to represent the reduction of the circulation around the rotor blade. The reduction factor for a turbine of radius R and B blades at radius r from the hub was found by Prandtl to be

$$F = \frac{2}{\pi} cos^{-1}\left[exp\left(-\frac{B(R-r)}{2\,R\,sin\phi_R}\right)\right] \tag{2.40}$$

Where, ϕ_R is called the helix angle and defined as the angle made by the relative wind with plane of rotation at rotor tip.

Goldstein found the exact solution to flow problem about a lightly-loaded optimum rotor with a non-expanding wake using Bessel functions .This was compared with Prandtl's solution showing that the Prandtl's solution was very close to that of Goldstein's at high tip-speed ratios, and there was some amount of qualitative similarity at all tip-speed ratios. However, since an expanding wind

turbine wake is different from the constant-diameter wake of an optimum propeller, it is not apparent which model is more accurate [40]. It also important to realize that Glauert interpreted this tip loss factor not as a ratio of circulations but as a ratio of the average induced velocity at the annulus and the induced velocity at the blades. This was basically to simplify its application to BEM, without actually changing the expression. He also made this expression compatible with BEM by using the tip loss factor not for the entire rotor disk, but for each section of the blade in accordance with the strip theory approach of BEM. For this he used what can be termed as a local flow angle approach with the helix angle or the flow angle ϕ_R at the tip is replaced by the local flow angle ϕtaken at each section instead of the tip.

† the models developed by Bak et al. [62] and Powles [63], incorporate tower influence on the local velocity field.

† BEM theory uses an empirical relation for thrust on the annular actuator instead of a momentum balance when the section representing the actuator operates at or beyond the so called "turbulent-wake" state. At $a = 0.5$, the parabola in figure 2.13, which represents the thrust coefficient CT as a function of a reaches its peak value. Beyond $a = 0.5$, part of the flow in the far wake begins to propagate upstream and so the basic assumptions of momentum theory on a stream-tube do not hold. Hence, this relation is essential for high tip speed ratio

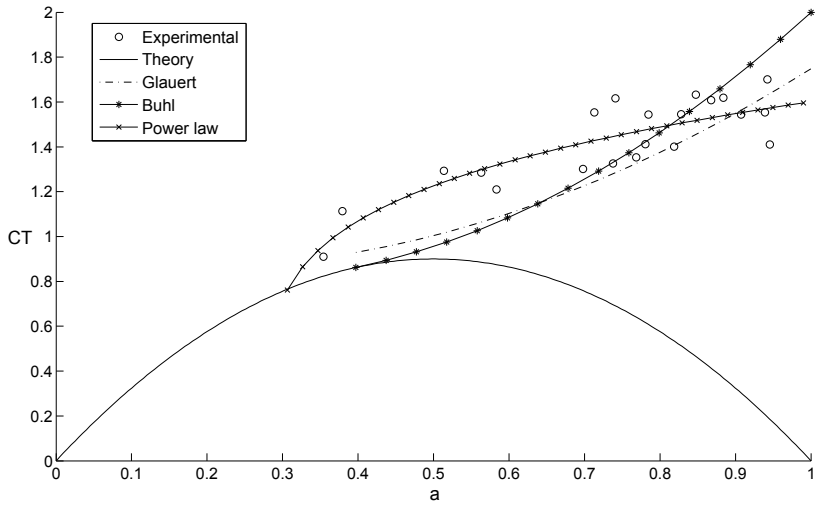

Figure 2.13: Thrust coefficient CT plotted against the axial induction factor a. The resulting parabola is a representation of the Momentum theory applied to a stream-tube in a typical BEM model; The empirical relations of Glauert [4] and Buhl [5] fitting data from experiments performed by Lock and Townend [6] and Munk [7] are also shown; lso added is the Power-Law fitting developed by Ponta et al. [8]. The parabolic CT curve shown here inlcudes the effect of tip-hub loss factor $f_{th} = 0.9$ to highlight the problem of discontinuity seen in Glauert's approach.

turbines for which the possibility of a going beyond 0.5 is quite high(for practical cases this value is generally taken to lie between 0.3 to 0.45). Glauert [4] was the first to propose such an empirical relation in the form of a fitted parabola. The parabola was fitted to data obtained from experiments performed on propellers by Lock and Townend [6]. Figure 2.13 shows that Glauert's function is tangent to the CT curve at $a = 0.4$. Others have proposed similar curves like Wilson [40] and Burton et al. However, if tip and hub losses are taken into consideration, the fitting curve is no longer tangent to the CT function. This results in a discontinuity at the point where the model must switch from using the momentum equation to using the empirical relation [5]. This can cause a problem during the iterative process solving for the induction factors, making

convergence difficult. Buhl [5] proposed using an empirical relation which forces the two curves to be tangential, whether or not the tip and hub losses are taken into account. The DRD-BEM model has the flexibility to switch between any of these models. More importantly, DRD-BEM has also incorporated a new Power-Law fitting [8]. This new curve significantly reduces the error in approximation compared to the experimental data. It also avoids any discontinuity since the Power-Law fitting always intercepts the stream-tube CT function in spite of the tip and hub loss corrections. This is another aspect of the BEM model that will be further explored in this dissertation.

A more comprehensive description of the standard DRD-BEM model can be found inPonta et al. [8] and the references therein. For the structural model thereader is referred to Otero and Ponta [29], which also includes the analysis of vibrational modes of composite laminate wind-turbine blades using the standard DRD-BEM model. Section 3 of Ponta et al. [8] presents results validating the standard DRD-BEM model with respect to the detailed results provided in Jonkman et al. [41] and Xudong et al. [64].

Inspite of all the modifications mentioned above owing to the two dimensional nature of the blade element theory, the force exerted in the radial direction by the rotor on the wind as it flows across it is not accounted for. As mentioned on several occasions, as the extent of rotor deformation out of the plane of rotation increases, the effect of

radial forces on the blade elements increases leading to the development of the 3-D DRD-BEM model which will be introduced in the next chapter.

Chapter 3

A 3-Dimensional DRD-BEM model

The 3-D DRD-BEM model aims at improving the accuracy with which to represent the forces involved in deflecting the stream-tube across the actuator disk for each blade section. Currently BEM, in all its implementations, takes into consideration the axial and tangential forces acting on the stream-tube, but not the radial component. The same is the case with DRD-BEM as shown in steps 2.4.5.4 to 2.4.5.5. In equation (2.32) the aerodynamic chord-wise and chord-normal forces acting on the blade section, represented by δF_{rel}, are projected from the coordinate system of the blade section to that of the hub giving δF_h. The force component in radial direction of the rotor plane (the plane where the annular actuator lies) is given by δF_{h_z} (see equation (2.33)). However, while equating δF_h obtained by the blade element theory to the rate of change in momentum across the actuator in equations (2.34)

and (2.35), while the axial and tangential forces are accounted for,the radial force δF_{h_z} is considered negligible. These radial forces are no longer negligible as blade flexibilty increases as does the misalignment of blade sections with the plane of rotation. This misalignment can also be caused by control actions. Therefore, it becomes important to include the radial component in the momentum balance for a complete representation of the 3-Dimensional interference of wind across the annular actuator.

One way to achieve this would be to add to the equations (2.34) and (2.35), another equation balancing the rate of change of radial momentum across the annulus. This could be done by adding another induction factor accounting for the change in the radial component of velocity due to the radial force on the stream-tube. However, this makes the coupling between axial and tangential induction factors more complicated. The robust and proven 2 equation iterative algorithm used so judiciously in the solution for the axial and tangential induction factors will have to be abandoned.

A less complicated approach would be to implement the momentum balance in a coordinate system that aligns with the blade section in the deformed configuration. As seen in equation (2.31), $\delta \mathbf{F}_{rel}$ has no span-wise component and since $\mathbf{C}_{Lthal}$ rotates around the spanwise z-axis, $\mathbf{F}_l$ will have no components in the span-wise direction either. The fact that the forces on an airfoil are represented by two components without a spanwise component is a consequence of the blade element theory. This ensures that the 3-Dimensional effects on interference induced by the radial forces,

as seen in the plane of rotation, is fully accounted for. Therefore the contribution of radial component will remain intact across the entire transformation between blade section and hub coordinate systems. An obvious advantage of such an approach is that while a 3-Dimensional interference pattern is obtained, the robust iteration procedure, used in the DRD-BEM method, can still be used since the aerodynamic force on the blade element still has only two components.

3.1 Extending the DRD-BEM to include 3-Dimensional interference

The above mentioned approach to obtain a 3-Dimensional interference pattern across the annular actuator, steps 2.4.5.1 to 2.4.5.6 will have to be reformulated. In order to understand the relationship between the blade element and the annular actuator representing that element, it would be helpful to refer to figure 2.1 just as was done while looking at the the DRD-BEM algorithm.

3.1.1 Modifying incoming wind across the annular actuator

As the undisturbed wind, $\mathbf{W}_{\infty wind}$ 2.1, flows across the annular actuator, instead of being projected onto the hub coordinate system, it is directly projected onto the

instantaneous coordinate system of the blade section, as follows

$$\mathbf{W}_{\infty l} = \mathbf{C}_{lL}\mathbf{C}_{Lb}\mathbf{C}_{\theta_p}\mathbf{C}_{\theta_{cn}}\mathbf{C}_{\theta_{az}}\mathbf{C}_{\theta_{tlt}}\mathbf{C}_{\Delta\theta_{yaw}}\mathbf{W}_{\infty wind}, \tag{3.1}$$

Here the orthogonal matrices perform the same coordinate system transformations as explained in DRD-BEM. Wind velocity, $\mathbf{W}_{l_{int}}$, obtained after interference by the annular actuator when aligned with the coordinate system of the deformed blade section is given by,

$$\mathbf{W}_{l_{int}} = \begin{bmatrix} W_{\infty l_x}(1 - a_l) \\ W_{\infty l_y} + \Omega\, r_h a_l{}' \\ W_{\infty l_z} \end{bmatrix}, \tag{3.2}$$

where a_l and $a_l{}'$, are, respectively, the induction factors representing the velocity fraction induced in the chord-normal and chord-wise directions of the airfoil section in the deformed configuration.

In accordance with equation (2.29) shown in section 2.4.5 we need to add to $\mathbf{W}_{l_{int}}$, the velocity components $\mathbf{v}_{str}$ and $\mathbf{v}_{mech}$ giving the velocity relative to the blade section as:

$$\mathbf{W}_l = \mathbf{W}_{l_{int}} + \mathbf{v}_{str} + \mathbf{v}_{mech}. \tag{3.3}$$

3.1.2 Projecting forces obtained by using the *Blade Element Theory* from the Lilenthal coordinate system to the blade section coordinate system

Following the same procedure as seen in Steps 2.4.5.3 and 2.4.5.4 the drag and lift forces are computed according to equation (2.30), giving the same $\delta\mathbf{F}_{rel}$ as that in equation (2.31). $\delta\mathbf{F}_{rel}$ is further projected onto the blade section coordinate system by

$$\mathbf{F}_l = \mathbf{C}_{Lthal}\, \mathbf{dF}_{rel}\, \delta l, \tag{3.4}$$

where $\mathbf{C}_{Lthal}$ is the orthogonal matrix which projects the aerodynamic forces (lift and drag) on to the blade section coordinate system i.e. the coordinate system aligned with the coordinates of reference line l. Since $\mathbf{C}_{Lthal}$ rotates the forces about the z-axis, the corresponding component of $\mathbf{dF}_{rel}$ in the z direction remains zero after the projection shown in equation (3.4).Therefore, $\mathbf{F}_l$ can now be written as

$$\mathbf{F}_l = \begin{bmatrix} \delta F_{l_x} \\ \delta F_{l_y} \\ 0 \end{bmatrix} = \begin{bmatrix} dF_{l_x} \\ dF_{l_y} \\ 0 \end{bmatrix} \delta l, \tag{3.5}$$

where $\mathbf{dF}_l = \mathbf{C}_{Lthal}\,\mathbf{dF}_{rel}$. dF_{l_x} and dF_{l_y} are the forces in chord-normal and chord-wise directions. These two components which will be used next for the momentum balance in the axial and tangential directions of the blade section coordinate system.

3.1.3 Equating the forces obtained from *Blade Element Theory* with those from the *Momentum Theory*

In 3-D DRD-BEM the momentum balance, unlike step 2.4.5.5, is now carried out in the blade section coordinate system. As explained earlier, only the chord-normal and chord-wise forces are considered in the BE theory, while the span-wise forces are assumed to be negligible. This ensures an aerodynamic interference which can still be represented by 2 interference factors, this time in the deformed blade section coordinate system. just as in equation (2.34), the axial component, δF_{l_x}, is equated to the momentum change on $W_{\infty l_x}$ associated with the axial interference factor a_l to give

$$dF_{l_x} = f_{th}\frac{4\pi\,\rho\,r_h}{B}\left(|W_{\infty l_x}|\,(1-a_l)\,W_{\infty l_x}\,a_l + (a_l{}'\Omega\,r_h)^2\right) \tag{3.6}$$

in addition to the change in velocity and force components, the other changes in equation 3.6 with respect to equation (2.34), are the absence of the factor $\frac{\delta r_h}{\delta l}$ and

the splitting up of $W^2_{\infty l_x}$. $\frac{\delta r_h}{\delta l}$ accounted for the fact that the blade element length (corresponding to the thickness of the annular actuator) must be projected from the blade section coordinate system to the hub-coordinate system. This is not required anymore, as the actuator is no longer in the hub coordinate system but is instead already in the blade section coordinate system. $W^2_{\infty l_x}$ is split up to account for cases involving a relative wind velocity from the downwind side. Finally, the momentum change associated with the tangential induction factor $a_l{}'$ is equated with the tangential force component δF_{l_y} as follows

$$dF_{l_y} = f_{th}\,\frac{4\pi\,\rho\,r_h}{B}\,|W_{\infty l_x}|\,(1-a_l)\,a_l{}'(\Omega\,r_h) \tag{3.7}$$

3.1.4 Iterative process for calculating the induction factors

The iteration scheme used here is the same as that used in DRD-BEM. Similar to the process followed for a and a' the expression for a_l and a'_l can be written in an implicit way as

$$a_{l_{Res}} = dF_{l_x} - f_{th}\frac{4\pi\,\rho\,r_h}{B}\left(|W_{\infty l_x}|\,(1-a_l)\,W_{\infty l_x}\,a_l + (a_l{}'\Omega\,r_h)^2\right) \tag{3.8}$$

$$a' = \frac{dF_{h_y}\, B}{f_{th}\, 4\pi\, \rho\, r_h\, |W_{\infty l_x}|\, (1 - a_l)\, \Omega\, r_h} \tag{3.9}$$

Finally, $a_{l_{Res}}$ in (3.8) is minimized with the help of the adaptive algorithm explained earlier in step 2.4.5.6. Thus, the convergence criteria and error is, once again, monitored constantly by an efficient and extremely reliable numerical scheme [65, 66].

3.1.5 Computing the distributed loads on the blade

Steps 3.1.1 and 3.1.2 are repeated using the just calculated induction factors to find the aerodynamic load, dF_l, on each of the blade sections is calculated following. Finally as done in step 2.4.5.7, the aerodynamic moment as well as the gravitational loads are addded to the distributed forces and moments.

The corrective factors are implemented in exactly the same fashion as seen in the DRD-BEM model. It is important to point out that the tip loss correction is implemented in the same coordinate system as was done in DRD-BEM. This was done keeping in mind the derivation of the expression for the tip losses by Prandtl was done with the flow angle defined as that between relative wind and blade tip in the plane of rotation (see the Tip loss factors explained in section 2.4.6). The next chapter describes the numerical experiments performed to validate the 3-D DRD-BEM model. The chapter includes a detailed discussion of results of the said experiments

including a comparison with the results obtained using the DRD-BEM model.

Chapter 4

Numerical Experiments on 3-D DRD-BEM

In this chapter, results of the implementation of the 3-D DRD-BEM model for the aerodynamic analysis of a model *5-MW Reference Wind Turbine (RWT)* proposed by NREL [41] are presented. This model rotor is based on the REpower 5M wind turbine and was designed as a benchmark turbine for onshore as well as offshore installations. It is a good representation of state-of-the-art, utility-scale, multi-megawatt commercial turbines. The results are compared against those of the standard DRD-BEM model. Based on the discussions in previous sections this new implementation comes into its own when the out of plane deformation of the blade sections are significant.

Keeping this in mind the numerical experiments presented in this chapter were designed for a range of modifications of the NREL-RWT turbine. The modifications consited of varying the hub-coning angle (θ_{cn}) from 0° to 20° and also stiffness of thge blade from hyper-stiff to 60% more flexible than the standard one. To create a blade which is hyper-stiff a standard blade's stiffness was increased by a thousand timesin order to create a rotor in which deformations were essentially negligible. This made it easier to single out the effects of blade deformation on the interference patterns. The reduction in flexibility, on the other hand, was brought about by a gradual reduction of the blade stiffness and blade mass of the standard NREL-RWT blade by 10%, 20%, 30%, 40%, 50% and 60%. These rotors with modified blades and varying θ_{cn} are compared with the standard configuration. This is done for both the models i.e. standard DRD-DEM as well as the 3-D DRD-BEM model. Tilt and gravitational loads were not included in the initial experiments, essentially to use a steady-in-time solution to help understand the effects of misalignments using an organized and step by step process. Finally, tests including gravity and tilt were conducted (section 4.3). The results show a definite improvement in the the new model's ability to incorporate the 3 dimensional interference of the rotor into the momentum equations.

4.1 A 3-D interference pattern

In this section the effects of exchange of momentum in the radial direction of the plane of the rotor is highlighted. The results presented here are based on Hyper-stiff blades mentioned earlier with a conicity θ_{cn} of 10° and 20°. As explained in the last section, hyper-stiff blades will help single out the effects of out-of-plane deformations, which in this case are being introduced artificially by the variation θ_{cn}.

The results shown in figure 4.1 represent the power coefficient C_P as a function of tip speed ratio λ. Results from the standard DRD-BEM model are depicted by dash lines and those from the 3-D DRD-BEM model are represented by solid lines. As expected, at a tip speed ratio of about 8 all of the cases attain the maximum power that the turbine can extract. Looking at the plots, two important differences can be seen in the results given by the standard model and the 3-D model. The first thing that can be noticed is the drop in C_P obtained by the 3-D DRD-BEM model. This is because the new method includes the forces acting in the rotor planes radial plane, thereby increasing interference and reducing the available flow kinetic energy. The second significant difference is how the gap in the results obtained by the two models increases with an increase in θ_{cn} from 10° to 20°. This can be explained by the expected increase in the contribution of radial forces as the extent of misalignment of the blade sections with respect to the plane of rotation increases with increase in θ_{cn}.

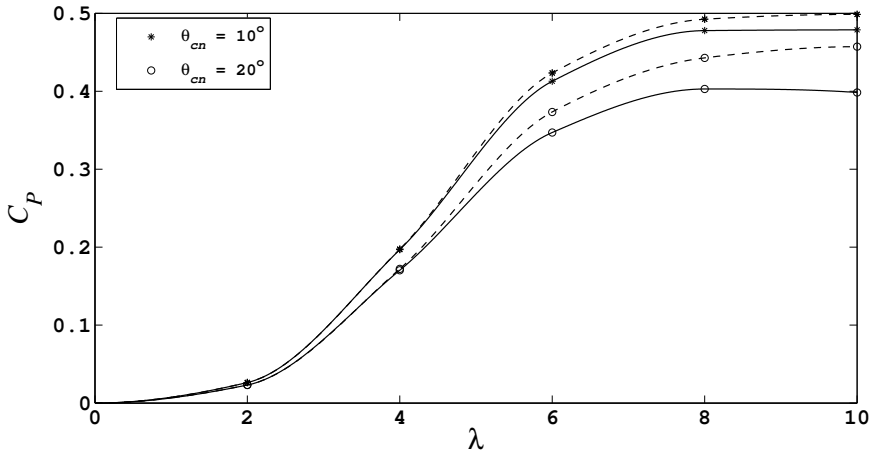

Figure 4.1: C_P Vs λ for a coning angle $\theta_{cn} = 10°$ and $\theta_{cn} = 20°$. The dashed lines represent the standard DRD-BEM model and the solid lines represent the 3-D DRD-BEM model

The plots in figure 4.2 highlight the contribution of radial forces in a more direct fashion. Figure 4.2 shows a comparison of the absolute value of the tangential induction factor a' as obtained both by the two models after projecting them onto the h-coordinate system. A third induction factor a'' is also added to the plots. This induction factor represents the change in wind velocity in the radial direction of the rotor plane. The figure on top represents $\theta_{cn} = 10°$ while the one below is for $\theta_{cn} = 20°$.

It is worth mentioning that this third induction factor a'' is not actually calculated in the 3-D DRD-BEM model, since, as explained earlier introduction to 3, the momentum equation is solved in the l coordinate system (also referred to as the deformed blade section coordinate system) which is aligned with the deformed blade section. Therefore, a need to solve for a third induction factor never arises in either of the

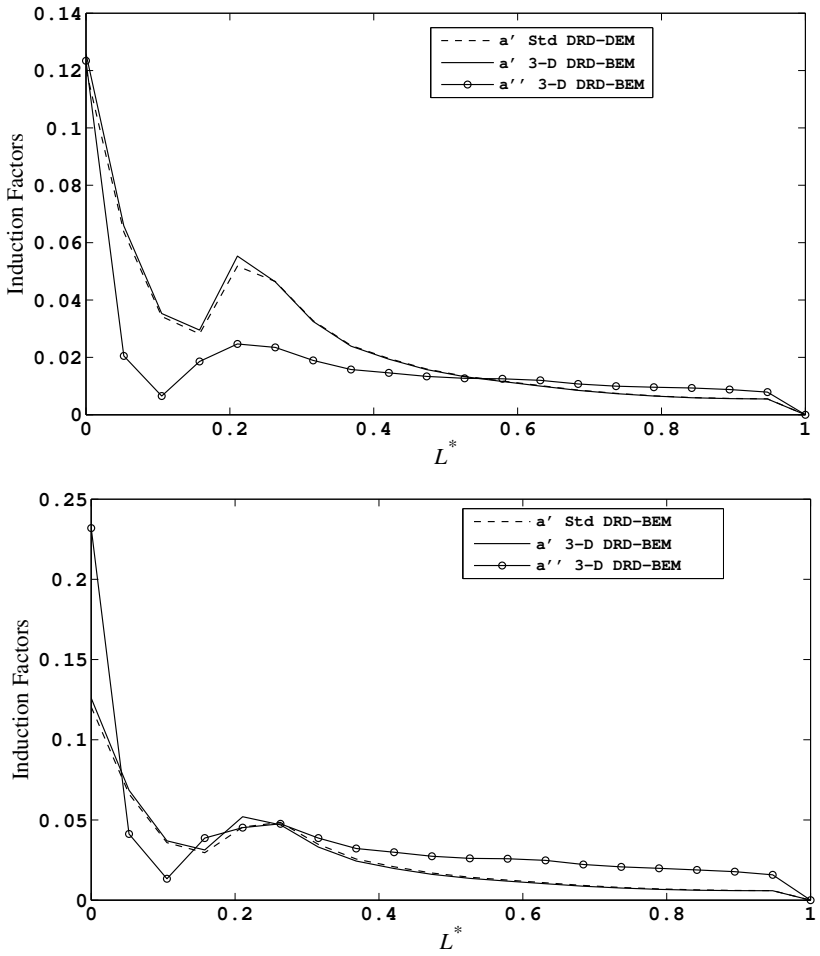

Figure 4.2: a' using the standard DRD-BEM (dashed lines) and the 3-D DRD-BEM (solid lines) and a radial induction a'' obtained by the 3-D DRD-BEM, as a function of the normalized blade length L^*. All three induction factors are projected on to the h-coordinate system. In the figure on top $\theta_{cn} = 10°$, while for the one below $\theta_{cn} = 20°$

two models. Here, however, this induction factor was extracted specifically for highlighting the effect of radial forces with increasing levels of rotor misalignments. Thus, this new "radial" induction factor illustrates how an annular section of the rotor acts upon the incoming wind in the radial direction of the hub coordinate system.

Figure 4.2 shows that the tangential induction factors obtained by either method are

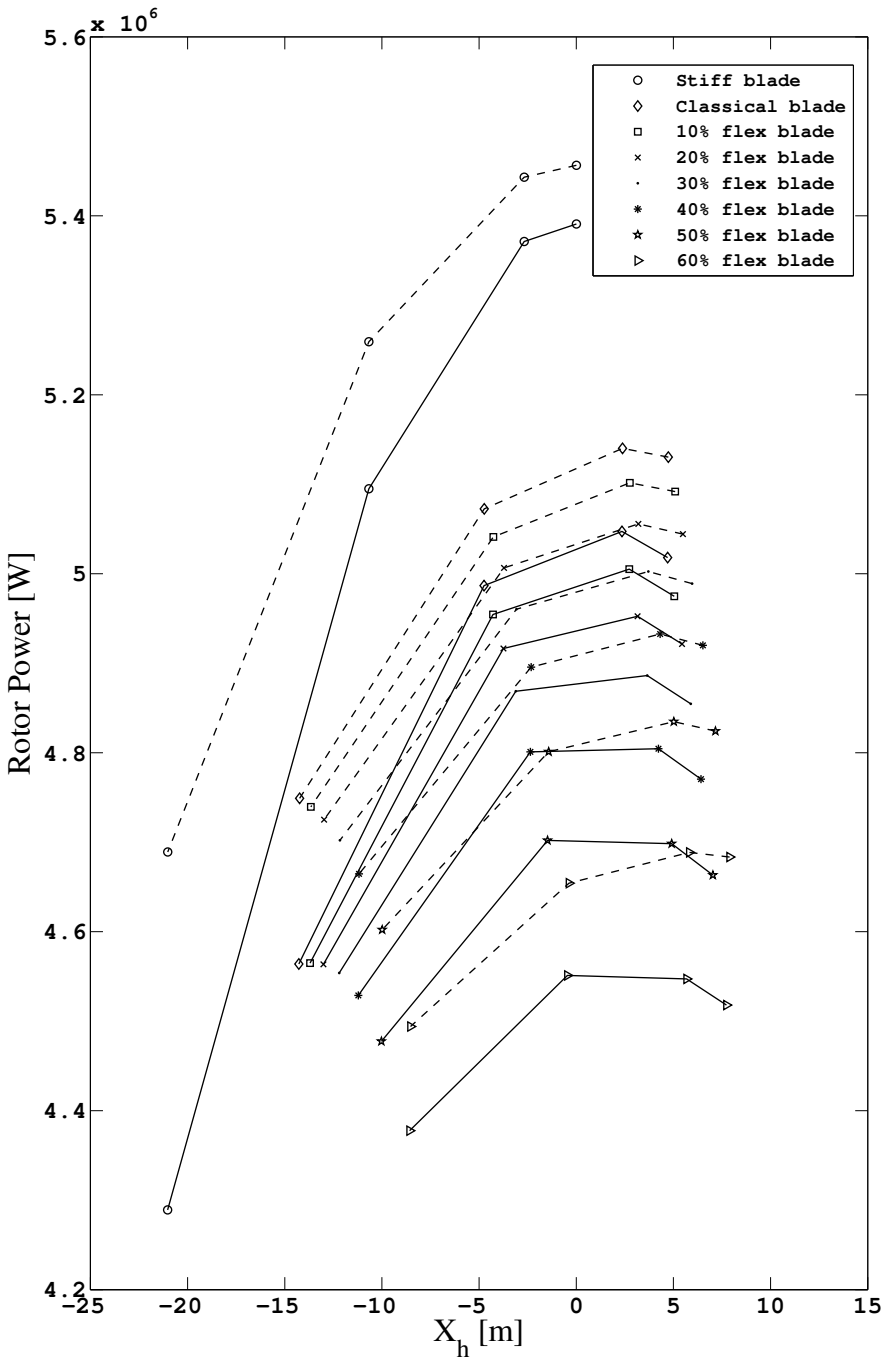

Figure 4.3: Rotor power as a function of Tip-displacement x_h. Dashed lines represent standard DRD-BEM results and solid lines represent the 3-D DRD-BEM results

similar. The slight difference can be explained by a more general 3-D interference pattern taken into account by 3-D DRD-BEM. The a'', however, can be seen to play a significant role in causing the divergence in C_P values shown in figure 4.1. From the two plots it can be seen that as far as the magnitude is concerned a'' is comparable to a'. Also, as θ_{cn} increases, the contribution of radial forces also increases, as evidenced by a significant increase in a'', which is now greater than a' over a major portion of the turbine blade.

4.2 Effect of misalignment on Rotor Power

For the plots shown in figure 4.3 only the aerodynamic loads were considered. This was done to highlight the fact that the sensitivity of the 3-D DRD-BEM model to aerodynamic loads increases when compared to the standard DRD-BEM model. Figure 4.3 represents the power output of the rotor against the distance of the blade tip from the plane of rotation along the x-axis of the h-coordinate system. The results are shown for one blade since all three blades will follow the same steady-in-time response over each cycle. As before, the 3-D DRD-BEM results are represented by solid lines and the dashed lines for the standard DRD-BEM results. Power is plotted for blades with increasing flexibity, beginning with the hyper-stiff blade followed by the standard NREL-RWT blade and finally the set of six flexible blades defined earlier. The points on the curves represent an increasing coning angle θ_{cn}. It starts at 0°, followed by

the design conicity of 2.5° and finally higher coning angles of 10° and 20°. The x-axis should, therefore, account for blade deformation as well as misalignment due to varying θ_{cn}.

The first two curves in figure 4.3 are for the hyper-stiff blade. The standard DRD-BEM results are represented, once again, by the dashed line and those of the 3-D DRD-BEM model by the solid line. This scheme of solid and dashed lines is followed in the remaining curves in the figure 4.3. The difference in results obtained by the two models increases significantly for higher θ_{cn}. The point at $x_h = 0\,m$ represents $\theta_{cn} = 0°$ and that at $x_h = -21.03\,m$ represents $\theta_{cn} = 20°$. This results from increasing conicity leading to higher levels of rotor misalignment with the plane of rotation. With increasing flexibility, a drop in rotor power can be noticed. This can be explained by complex modes of deformation expected of flexible blades being better captured by a more sensitive BEM model. Also, with the contribution of radial forces being accounted for, the momentum lost in the radial direction is also accounted for, and this takes away from the contribution of the momentum carried by incoming wind to power output. Another important aspect seen in the plot is the relative difference in power between the two models when $\theta_{cn} = 0°$. This difference clearly increases with increase in rotor flexibility. This is due to the fact that more flexible blades will deform more from the plane of rotation and hence the contribution of radial forces will also increase. Therefore, the 3-D DRD-BEM model is better at capturing the effects of out-of-plane attitude of blade sections. It can also be seen that, for power

output at higher θ_{cn}, the gap between the two curves decreases at first. At first, for the 3-D DRD-BEM results, the region between $\theta_{cn} = 2.5°$ and $\theta_{cn} = 10°$ flatten out as flexibility increases. However, it finally begins to increase again. This is to be expected since the misalignment due to blade deformation opposes the misalignment due to an increase in θ_{cn}. The net result is that the out-of-plane misalignment decreases as θ_{cn} increases in this region. As a result for θ_{cn} between 2.5° and 10°, x_h can be seen to lie around 0. x_h, however, increases as θ_{cn} moves towards 20°, increasing the contribution of conicity to misalignment. Therefore, the gap between the two models once again begins to increase for the region beyond $\theta_{cn} = 10°$. This could not be observed in the case of the hyper-stiff blades. This can be explained by the fact that the deformation in that case is negligible, so only θ_{cn} is responsible for causing any misalignments. These factors reflect the versatility and higher sensitivity of the 3-D DRD-BEM model in capturing complex effects of rotor deformation on the computation of aerodynamic loads.

4.3 Time-dependent solutions around the nominal operational state

Results for time-dependent solutions are presented in this section. Results obtained by the two models are compared in terms of power output, rorot thrust and displacement

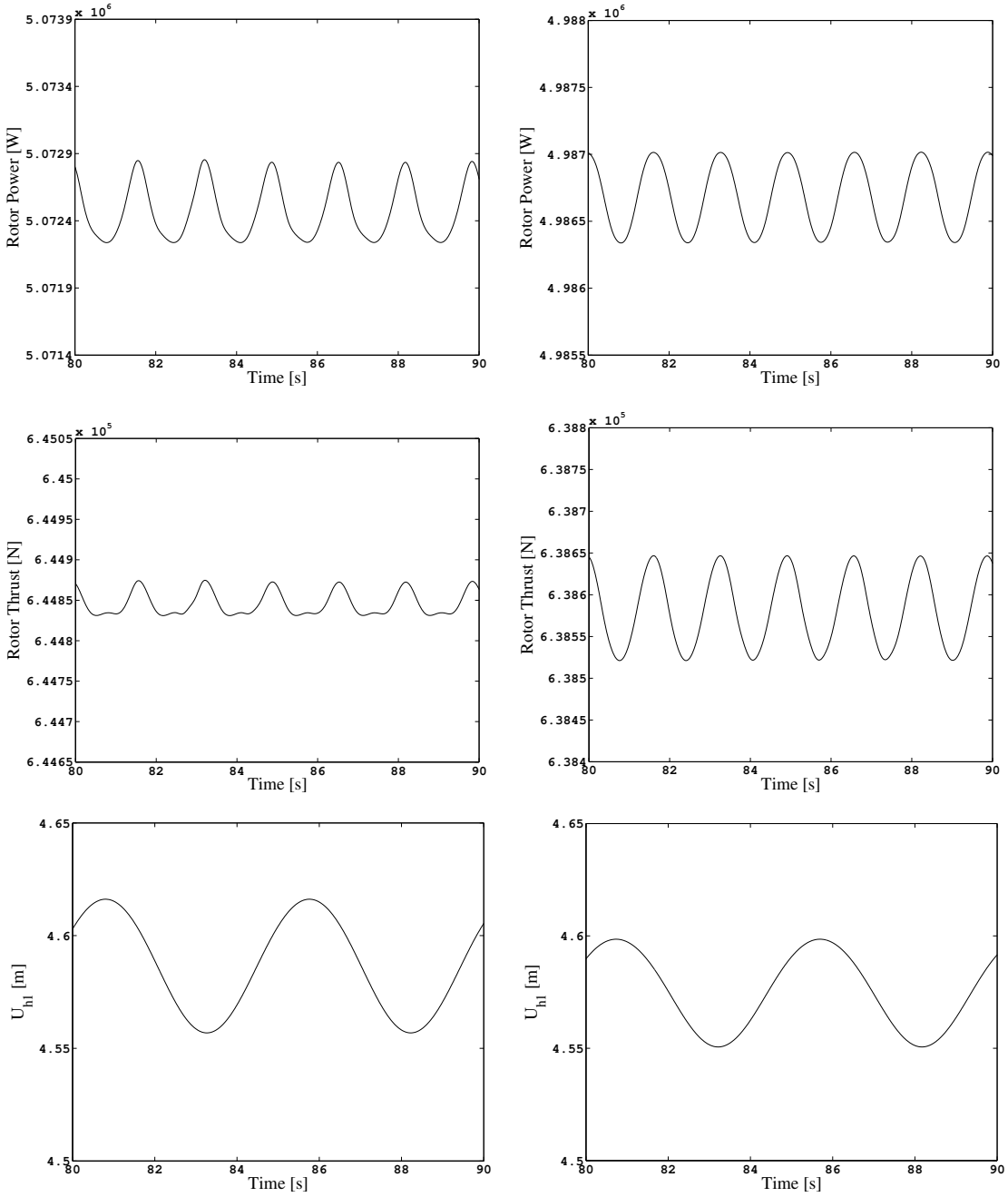

Figure 4.4: Time dependant solutions for a standard NREL-RWT with only aerodynamic loads accounted for, with $\theta_{cn} = 10°$. The left hand column shows the standard DRD-BEM results, while the right hand column shows the 3-D DRD-BEM results

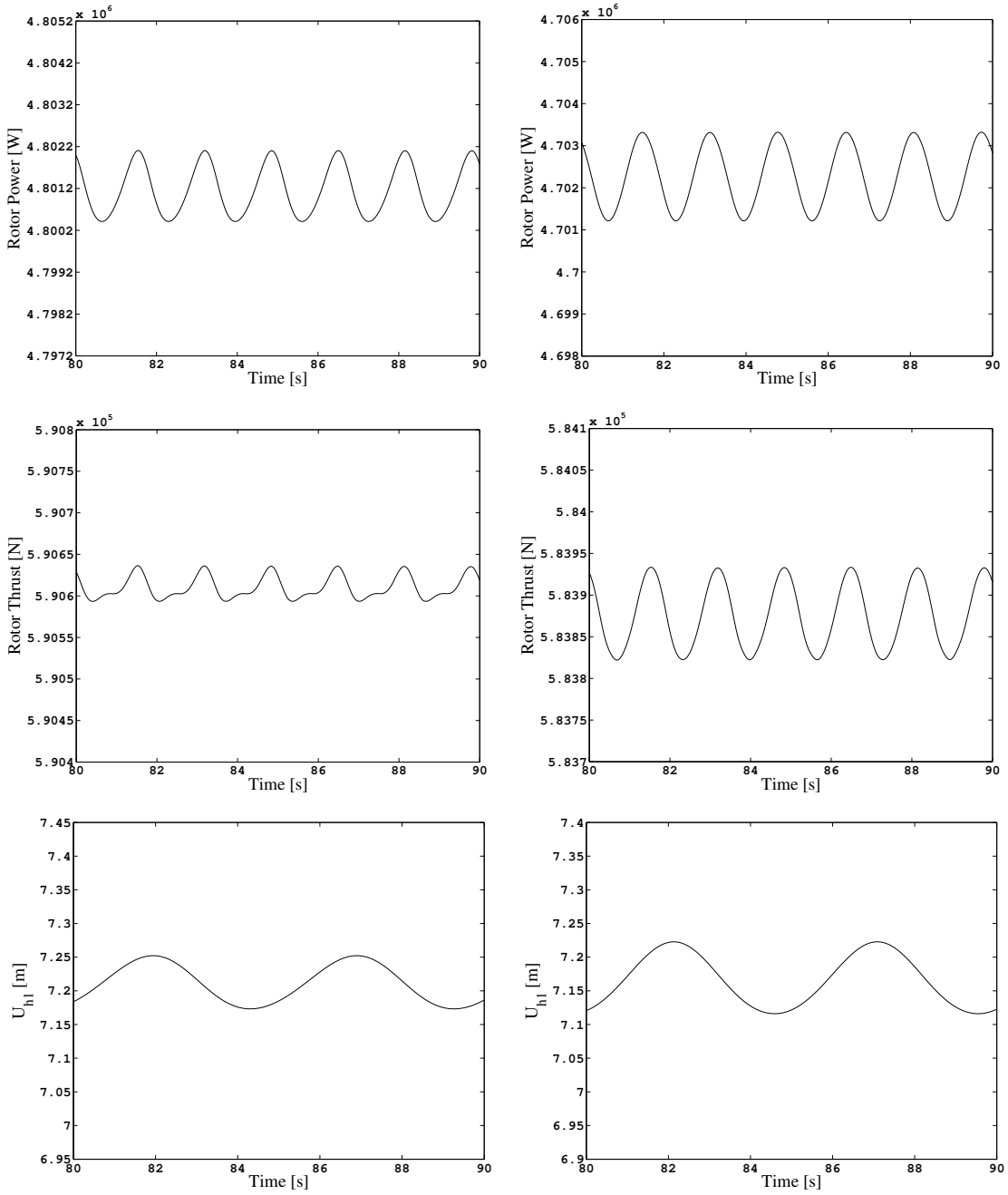

Figure 4.5: Time dependant solutions for a blade 50% more flexible than the standard blade and $\theta_{cn} = 10°$. The left hand column shows the standard DRD-BEM results, while the right hand column shows the 3-D DRD-BEM results

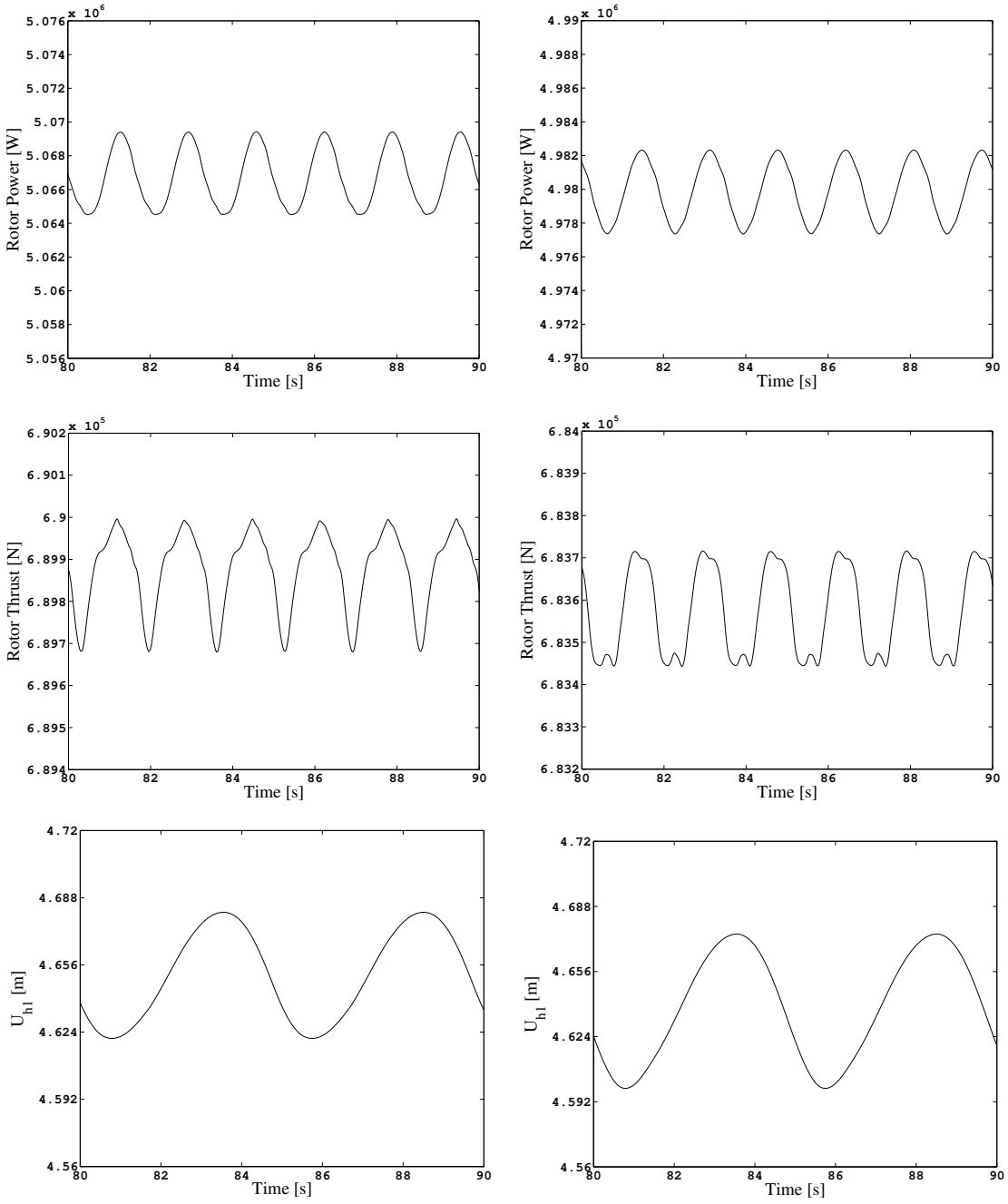

Figure 4.6: Time dependant solutions for a standard NREL-RWT with both aerodynamic and gravitational loads accounted for and $\theta_{cn} = 10°$. The left hand column shows the standard DRD-BEM results, while the right hand column shows the 3-D DRD-BEM results

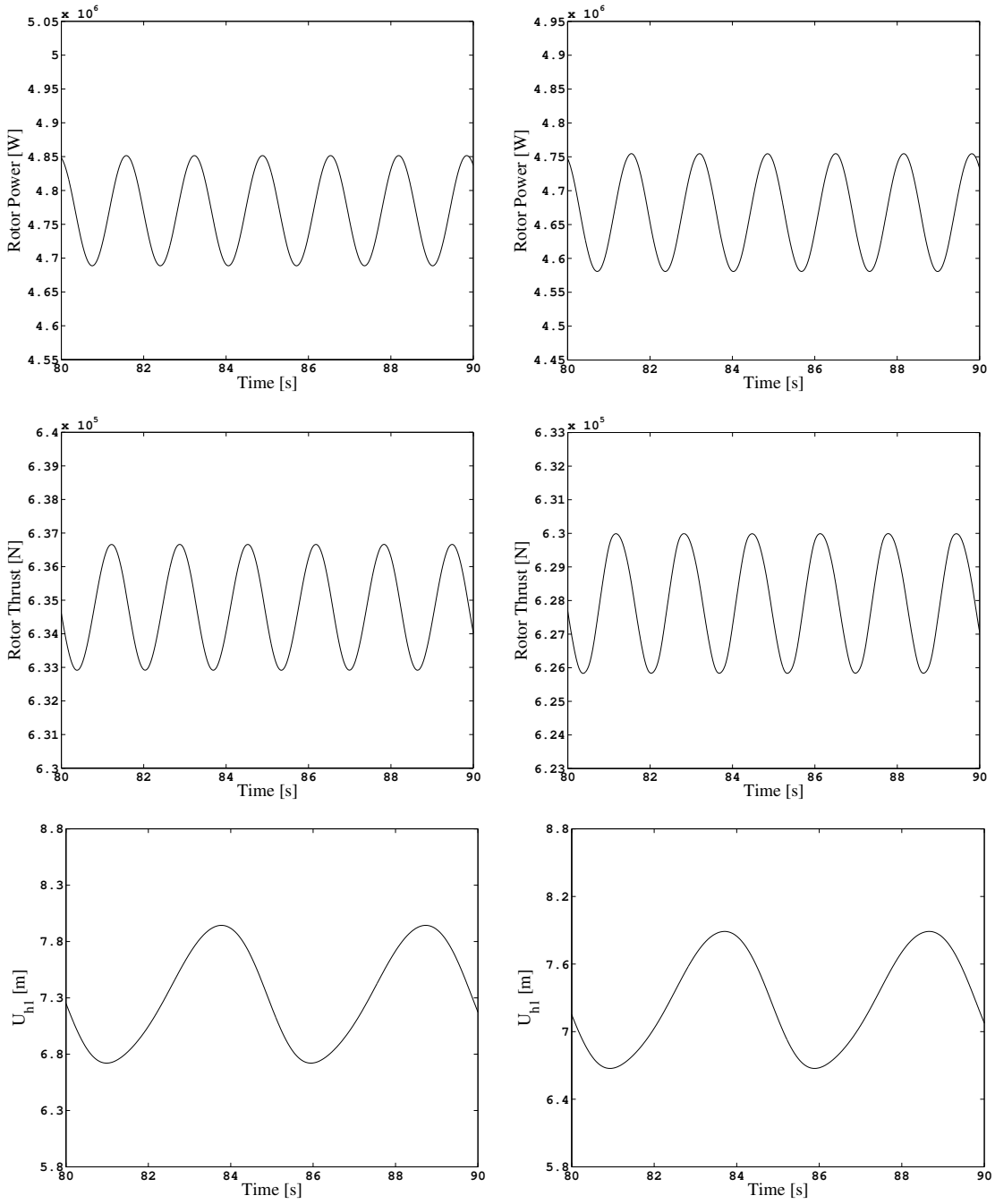

Figure 4.7: Time dependant solutions for a blade 50% more flexible than the standard blade with both aerodynamic and gravitational loads accounted for and $\theta_{cn} = 10°$. The left hand column shows the standard DRD-BEM results, while the right hand column shows the 3-D DRD-BEM results

of the blade at 90% length. Figures 4.4 and 4.5 include the effects of aerodynamic loads only. The oscillatory nature seen in the plots are due to the design tilt of 5° and for figures 4.6 and 4.7, in addition to tilt, there is the added effect of gravitational loads, both of which introduce asymmetries into the solution. This allows for testing the 3-D DRD-BEM model for unsteady aero-elastic effects. While the simulation was run for 100 seconds, the results are shown only for a window of 80 seconds to 90 seconds.

In figure 4.4 the simulation results for a standard NREL-RWT blade are presented. In the results it is observed that all variables obtained by using the 3-D DRD-BEM model show a reduced mean value, which, in accordance with results shown in previous sections, is due to the effects of the radial force component included in the new model. Another valuable observations is made in the plots showing rotor thrust. The thrust plots clearly depict an increased sensitivity to misalignment for the 3-D DRD-BEM model. Figure 4.5 includes results for blades with flexibilty increased by 50%. These plots show similar trends, with the increase in sensitivity now evident for all the variables plotted. This was also to be expected as greater flexibility must result in greater deformation which in turn will lead to higher levels of misalignment. This would cause an increase in the contribution of radial forces, which is, as expected, better captured by the 3-D DRD-BEM model. Figures 4.6 and 4.7 represent similar cases with the only addition being inluding the effects of gravitational loads.

Chapter 5

The Actuator Disk Model

All of the misalignments highlighted in previous chapters, intended to be accounted for by the 3-D DRD-BEM model, cause changes in effective velocity at different sections of the rotor. Since these misalignments are expected to be at a larger scale in modern turbines, this can lead to high axial induction factors at certain blade sections. Some situations most prevalent in modern wind turbines, leading to significant levels of misalignments, are the transitional states between control actions, especially pitching action which takes a finite amount of time given the inertia presesnted by extreme blade sizes [30, 31]. Another example would be a turbine being operated in a deloading state [32, 33, 34, 35, 36] as shown in figure 5.1. Other important cases are extreme wind condtions consisting not only of gusts but also low winds, given that wind turbines are operating in a much wider range of wind conditions than earlier [38].

There are a few more situations mentioned in the introduction with relevant references cited.

Figure 5.1 shows a possible scenario where the flow might enter states of axial induction factors greater than 0.5. Figure 5.1 represesnts a situation where the turbine is operating at a deloaded condition for the case of below nominal wind speed of $6m/s$ by increasing the rotor RPM from approximately 8 RPM to 10 RPM. The range of optimal RPMs for the given wind speeds for an NREL 5MW turbine can be found in [41]. An RPM of 10 was decided upon based on the works of [67] which includes an analysis of deloading an NREL 5MW reference turbine and [68] which presents an analysis of deloading control strategy and feasible limits of RPM variation used for deloading.

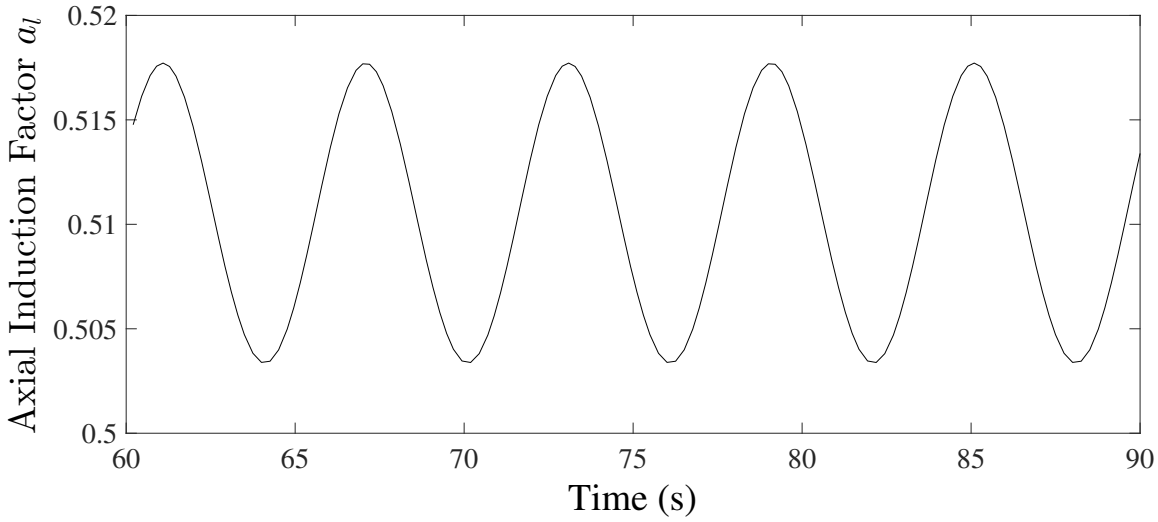

Figure 5.1: Axial induction factors, at 90% span, for an NREL 5MW reference turbine operating in a deloaded condition of 10 RPM at a wind velocity of $6m/s$ instead of the usual 8 RPM.

The one dimensional momentum model, as used in BEM, is no longer reliable across an actuator disk in this regime. As such there has been substantial analysis of these flow states with regard to the BEM model. Lock et al. [11] provides one of the earliest detailed analysis of these states, and proposes a possible empirical correction based on experiments. Several other authors who have provided a detailed analysis of these states include Burton et al. [2], Stoddard [69, 70], Eggleston and Stoddard [9], Wilson and Lissaman [71] and Glauert [4] whose work forms the basis of the correction model used in BEM. More recent analysis can be seen in Sørensen et al. [72], where a numerical analysis of an actuator disc model for the flow states seen in this regime is presented and Johnson [73] providing a detailed review of various experiments providing data for these flow states. The normal operating state of the rotor is called the windmill brake state where the rotor extracts energy from the flow. As the tip speed ratio increases either due to a change in orientation or a drop in wind velocity (relative or otherwise), the axial load on the rotor increases, thereby, increasing thrust and consequently the axial induction factor. Initially the rotor starts to see some recirculation in its wake as flow from outside the wake mixes with the slow moving air in the wake. This is called the turbulent wake state where the rotor starts to act more and more as a circular disc. This, as seen in figure 5.2, occurs for an axial induction factor, a, ranging approximately from 0.5 to 1. For even higher values of a, the rotor enters the vortex ring state, where the recirculation now assumes a toroidal path centered at the tip of the rotor disc. Finally the flow across the rotor reverses

and the turbine starts acting like a propeller imparting energy into the flow while still creating thrust in a downwind direction. This state is called the propeller brake state. Figure 5.2 represents these states with respect to the theoretical parabolic curve as obtained by the momentum theory. The experimental results used by Glauert [4] are also shown in figure 5.2. It is this set of data that this study aims to improve upon with the help of a numerical experiment as dicussed next.

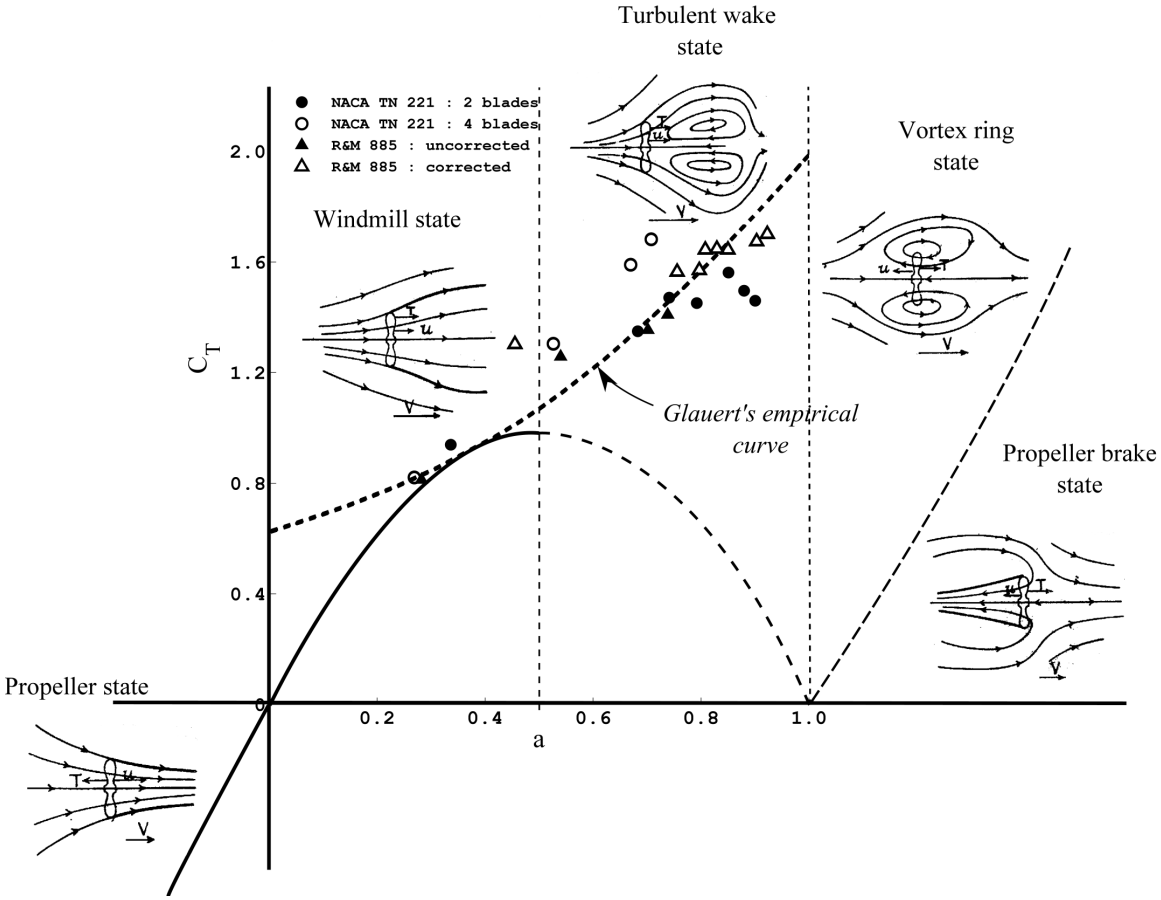

Figure 5.2: Thrust coefficient versus axial interference factor 'a' with various operating flow states of a wind turbine based on figures from [9] and [10]. The flow states from Lock et al. [11] show induced velocity 'u' at the rotor, free stream velocity 'V' and thrust 'T'. The figure is not to scale.

The numerical experiment consists of a 2-D Actuator disk model simulating flow across an annular actuator. In a BEM model each blade section is represented by an actuator disk, in the form of an annular actuator, for the purpose of performing a momentum balance across it. However, as explained previously, for high axial induction factor regimes we need a more complex analysis than a simple 2-D momentum balance. This analysis was performed by using data from experiments on propellers by Munk [7], Lock and Bateman [39] and Lock et al. [11] by Glauert [4] and Lock [11]. Glauert was the first to propose using an empirical fitting to the experimental data for a BEM model. He proposed to interpolate a thrust value based on the fitting for high induction factor flow states, rather than using a momentum balance. This method, as previously mentioned, has since been widely accepted with several researches introducing slight modifications to the original empirical relation proposed by Glauert. We propose using data from a simulation, rather than experiments, to perform the analysis for such flow states. This is primarily because a BEM model is based on a momentum balance across an ideal actuator disk. Therefore, a 2-D actuator disk model is more representative of the BEM theory. So each section is still an actuator disk, only the simple 2-D momentum balance is now replaced by a more complex turbulent flow actuator disk model for sections seeing high axial induction factors. Another factor which encouraged us to use a simulation model instead, was the substantial dispersion in data due to limitations of sensors used in that era as well as due to the unsteady nature, as expected, of a non-ideal case. The BEM theory

however, is based on a steady in the average momentum balance. Another factor is the increased sensitivity of 3-D DRD-BEM to changes in blade section orientation as seen in the results section of chapter 4, leading to the numerical solution seeing a wider range of axial induction factors. Hence there is a greater chance of the simulation entering flow states beyond the normal operating states. Another important point that needs to be reiterated is the fact that the the 3-D DRD-BEM operates in the l coordinate system. This means that the forces acting on the stream tube undergo only one small rotation about the z axis, unlike the extensive coordinate transformation required by DRD-BEM all the way to the h coordinate system. This means that the resulting induction factors seen in every iteration of the 3-D DRD-BEM will be the one seen in the l coordinates system and hence of a greater magnitude than the induction factors seen in the h coordinate system of DRD-BEM. This can be seen in figure 5.3 which plots a standard NREL 5 MW reference turbine operating at rated wind speed and rotor RPM, for a duration of 90 seconds. The solid line representing the axial induction factor seen in 3-D DRD-BEM can be seen to be much higher than the axial induction factor of the DRD-BEM algorithm represented by the dashed line. This difference is expected to get higher for cases with greater misalignments. This makes it all the more important to pay special attention to these flow states for a 3-D DRD-BEM model.

In light of all of these factors, a 2-D actuator disk analysis for the high axial induction factor flow states was performed. The model was created in Ansys Fluent and a $k-\epsilon$

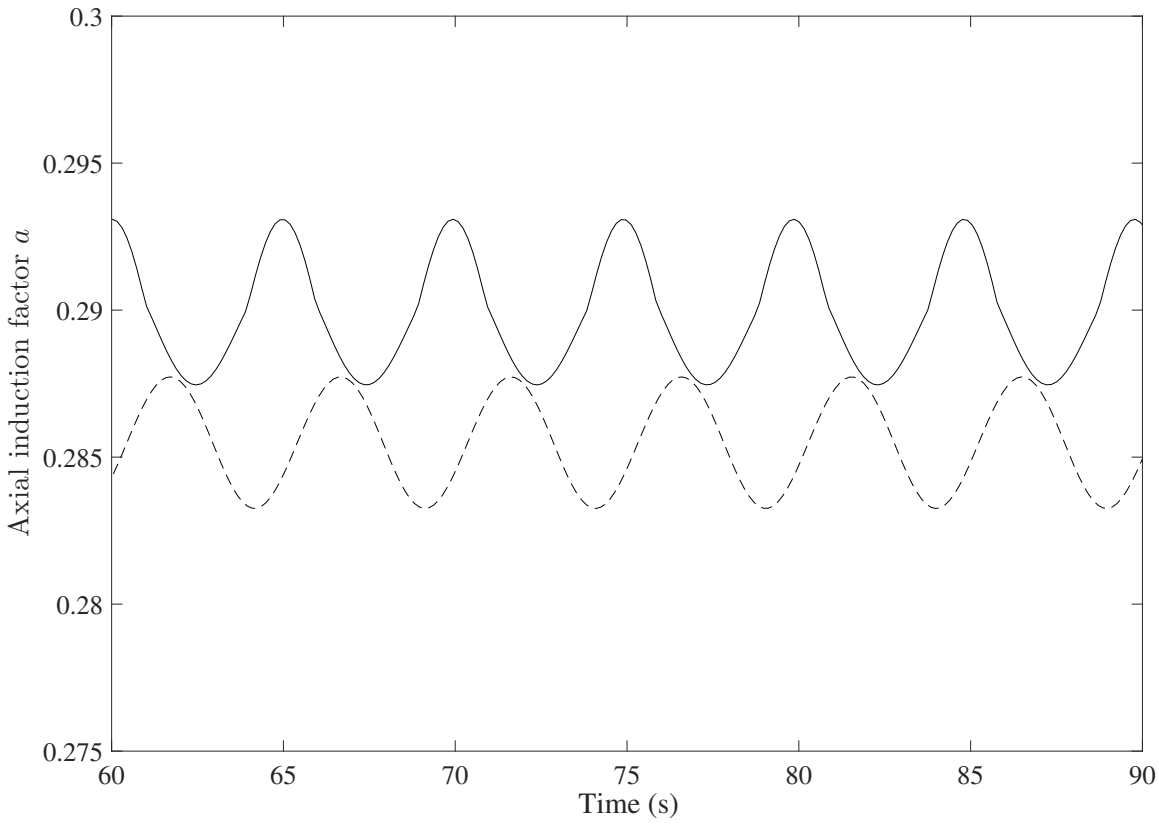

Figure 5.3: Axial induction factors, at 90% span, for an NREL 5MW reference turbine under normal operating conditions. The solid line represesnts the axial induction factor a_l obtained by the 3-D DRD-BEM method, while the dashed line shows the axial induction factor a as obtained by DRD-BEM.

realizable turbulent model was used.

5.1 The numerical experiment

The actuator disk model created in Ansys-Fluent consists of an axisymmetric domain, with the actuator disk being represented by an infinitely thin boundary in the form of an interface between cells. This interface acts as an actuator disk by virtue of a

discontinuous pressure drop applied across it. It, therefore, represents a uniformly loaded actuator disk, which is what each annular strip of BEM represents. The flow was solved using a $k-\epsilon$ realizable turbulence model. As mentioned in [74] and [75] the $k-\epsilon$ models unlike the $k-\omega$ models are less sensitive to free stream properties of the turbulence kinetic energy and its dissipation rate. This is the reason why in the $k-\omega$ SST approach the model gradually changes from a $k-\omega$ formulation in the boundary layer to a $k-\epsilon$ one in the free shear regions. Since the above mentioned actuator disk model does not have to deal with boundary layers a $k-\epsilon$ model does seem to be the logical choice. The $k-\epsilon$ realizable model has been shown to perform better than other $k-\epsilon$ models for boundary-free shear flows with a high mean shear rate and flows with secondary flow features [74, 76]. All of these are the expected flow features in the actuator disk model for higher pressure drops. A comparison with the other turbulence models in Fluent showed that the results of the $k-\epsilon$ realizable model best matched the experimental data used by Glauert in the flow states beyond the turbulent wake state. It also seems to closely follow the trend of the polynomial fitting (suggested in DRD-BEM [8]) for the region between the Turbulent-wake state and the vortex ring state. This fitting has been shown to minimize the approximation error to Glauert's experimental data. Finally, the numerical experiment data merges perfectly with the theoretical solution of the Control-volume (CV) analysis for the low axial interference factor regimes. The validity of the CV analysis has been well established not just by controlled experiments in wind tunnels on propellers and

scaled models of turbines, but also in field measurements on full-scale wind turbines. Another important confirmation came in the form of the flow topology depicted in figure 5.4. Figure 5.4 shows that the case with an axial induction factor $a = 0.41$ for a $CT = 1.01$ shows the first signs of vortical wakes with recirculative patterns and re-entry flow (completely absent from the simulation model with $CT = 1$). It has been explained earlier how this flow pattern disrupts the stream-tube and makes the CV theory no longer applicable, thereby, entering the "Turbulent-wake state". This validates the choice of the turbulence model used to solve the actuator disk problem. What is interesting is the fact that this is also the point around which the data compiled by Glauert begins to enter the so called "turbulent wake state" (see figure 2.13). All these factors justified the use of a $k - \epsilon$ realizable turbulence model for our numerical experiments.

The pressure drop Δp across the actuator disk was based on the value of coefficient of thrust CT as seen by the propellers beginning from the regular operational states till the high axial induction factor states. CT is given by:

$$CT = \frac{T}{\frac{1}{2}\rho {W_1}^2 A} \tag{5.1}$$

Where A is the area of the actuator disk, Thrust $T = A\,\Delta p$, ρ is the density of air taken to be $1.225 kg/m^3$ and W_{infty} is the free stream velocity.

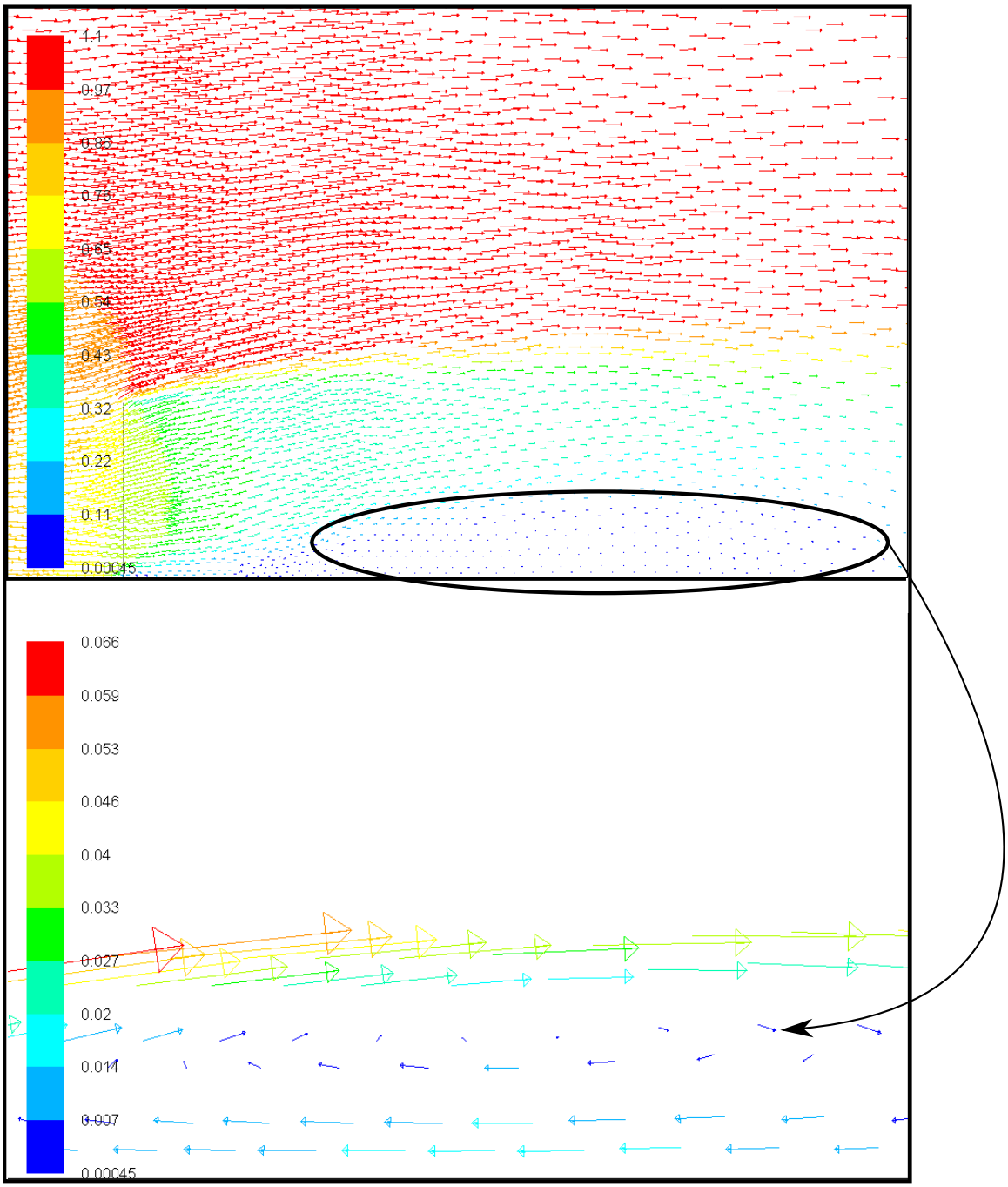

Figure 5.4: Figure on the top panel shows the wake behind the Actuator Disk at $CT = 1.01$. Recirculation can be seen in the zoomed in region shown in the bottom panel.

Therefore, the pressure drop Δp across the actuator disk can be found from the CT values using:

$$\Delta p = \frac{1}{2}\rho\, CT \tag{5.2}$$

The pressure drop Δp was found for CT values ranging from 0.2 to 4. These Δp values were applied across the actuator disk model in Fluent and the respective axial induction factor across the disk was calculated. The induction factor was calculated using the relation $W_2 = W_1(1 - a)$, where W_1 is the free-stream velocity and W_2 is velocity at the disk. W_2 is found by performing an area weighted average of the axial velocities at the actuator disk cells.

5.2 Results and discussion

The axial induction factors obtained from the Actuator disk model were then plotted against the respective CT values to get the plot in figure 5.6. Table 5.1 shows a sample of the data used in figure 5.6. To be used in the 3-D DRD-BEM algorithm explained in chapter 3, a 4^{th} order polynomial is used to fit the data (also shown in 5.6). This polynomial will be used to find the CT value once the axial induction factor goes beyond 0.28. An axial induction factor of 0.28 was chosen based on where the curve obtained from the model begins to depart from the theoretical curve.

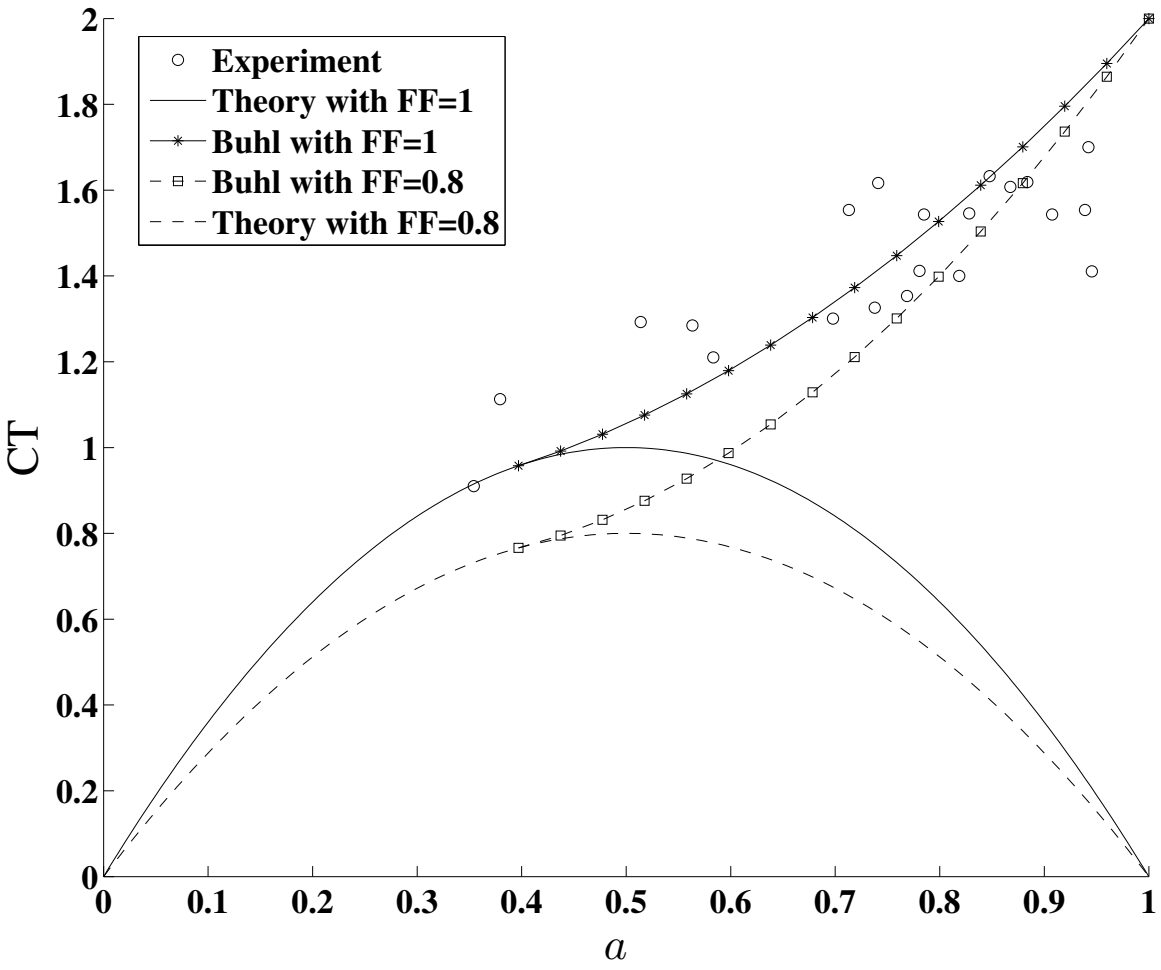

Figure 5.5: Comparison of Buhl's fitting with no tip-hub losses i.e. $FF = 1$ shown as solid lines with a tip-hub loss factor $FF = 0.8$. shown as dashed lines

For finding the best fit curve, it was decided to use the entire set of data starting from $CT = 0.2$ till $CT = 4$ and not just for the data after $a = 0.28$. The reason for this lies in the definition of the tip loss factor. It was mentioned earlier that if tip and hub losses are considered a discontinuity appears between the CT function and the fitting curve [5]. For an iterative process this discontinuity has the potential to cause problems with convergence. Buhl's [5] solution was to force a tangential match with the stream-tube CT function whether or not the tip and hub losses are considered, but

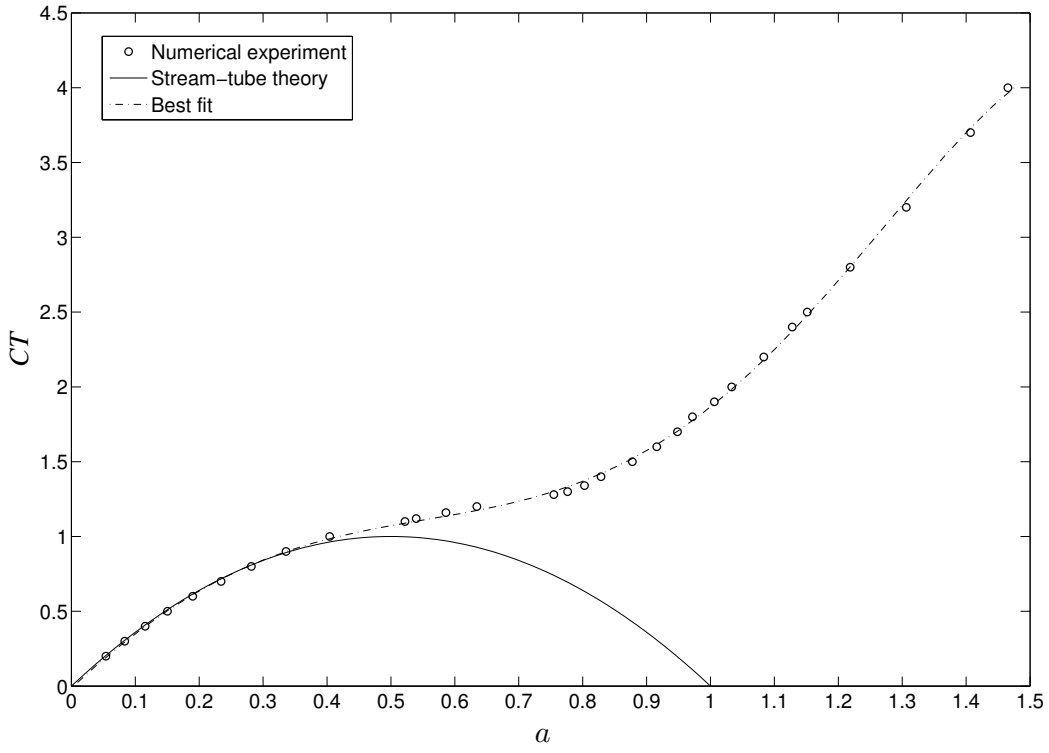

Figure 5.6: Coefficient of thrust CT as a function of the axial induction factor a.

in that process he ignored a lot of the initial data points from Glauert's experimental data set. To highlight this point, in figure 5.5 the fitting suggested by Buhl without any tip-hub losses are compared with a loss factor of 0.8 (an FF factor was also seen earlier in figure 2.13).

It can be seen that with the loss factor added Buhl's fit does not seem to follow the trend seen in the experimental data. Keeping this in mind it was decided to shift the entire fitted curve down by a factor equal to the Tip-Hub loss factors. This, however, dramatically shifted the point at which the fitting curve departed from the theoretical one. The solution to that inherently lay in the way the best fit curve was derived. It

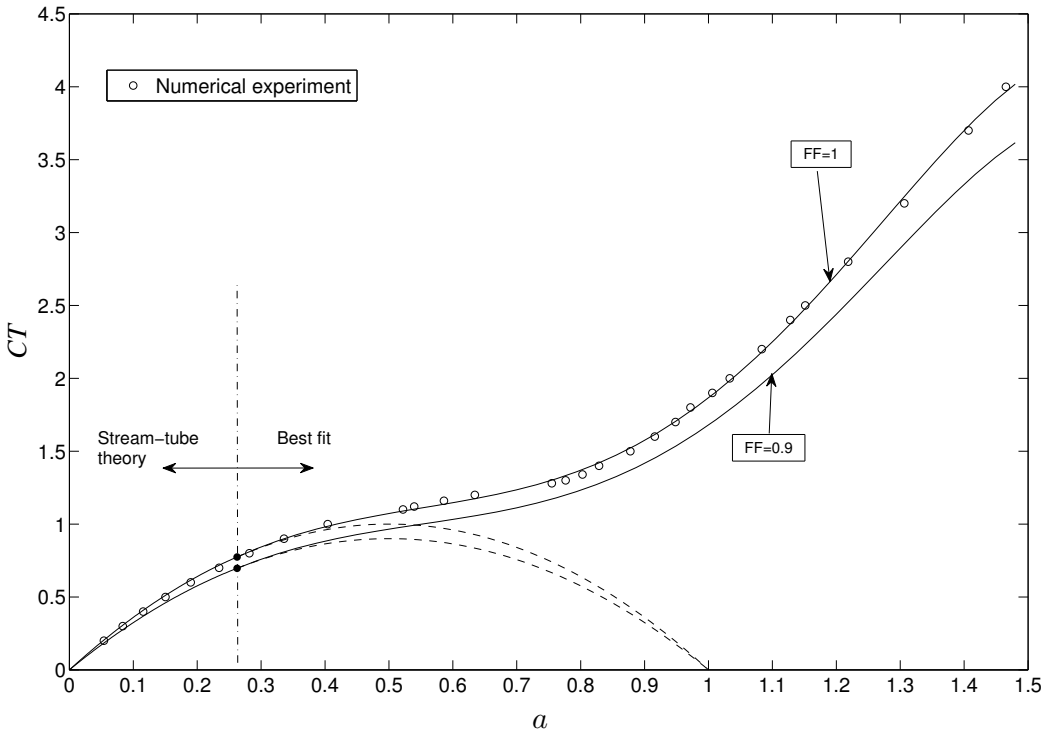

Figure 5.7: Coefficient of thrust CT as a function of the axial induction factor a FF=1 and FF=0.9.

was decided to use the entire set of data starting from $CT = 0.2$ till $CT = 4$ and not just for the data after $a = 0.28$. Using the entire data set not just ensures that the point of departure always lies at $CT = 0.28$, but also makes sure that the accuracy of the control volume analysis, which has been proven time and again, is fully utilized.

Figure 5.7 shows the plot obtained by the above mentioned fitting procedure. Of the two fitting curves in the plot, the one on top represents the case where no tip-hub losses have been included. The one below that curve is for a tip-hub loss factor of 0.9 and can be seen to pass through $a = 0.28$ just as the one without any loss factor.

The following table 5.1 shows some of the data points obtained from the $k-\epsilon$ realizable

model of the actuator disk. The complete set of data used to obtain the new fitting can be in the table A.1 in Appendix A A

Table 5.1
Axial induction factor a given by the $k-\epsilon$ turbulence model for the pressure drop Δp applied across the disk. Δp is calculated based on the required CT value at the disk. W_2 is velocity at the disk.

Δp $[Pa]$	CT	$W_2\ m/s$	a
0.1225	0.2	0.05395	0.9461
0.245	0.4	0.11546	0.8845
0.3675	0.6	0.81019	0.1898
0.6125	1.0	0.59585	0.4042
0.735	1.2	0.36568	0.6343
0.8575	1.4	0.17135	0.8287
0.98	1.6	0.08405	0.9160
1.53125	2.0	−0.03326	1.0333
1.96	2.4	−0.12795	1.1280
2.45	2.8	−0.21853	1.2185
6.125	4	−0.46531	1.4653

The following figures show the implementation of the new interpolation in 3-D DRD-BEM when axial induction factor a_l, at 90% blade span, becomes greater than 0.4. As explained earlier, 0.4 is the point beyond which wake recirculation starts. The first case is for the start up region of the NREL 5MW turbine. Based on [41] a rotor RPM of 8.04 was used for a wind velocity of $6m/s$. The mean a_l over a one minute period is found to be 0.42. The second case is for a rotor rotating at $12.1RPM$ when the wind velocity suddenly drops to $5m/s$. The mean a_l over the same period is found to be 0.70. Figure 5.8 shows the two axial induction factors. The dashed line shows the start up zone of turbine operation, while the solid line represents the case where the wind velocity drops suddenly to $5m/s$. Figures 5.9 and 5.10 show the Power and Thrust of the rotor as well as the blade displacement at 90% span.

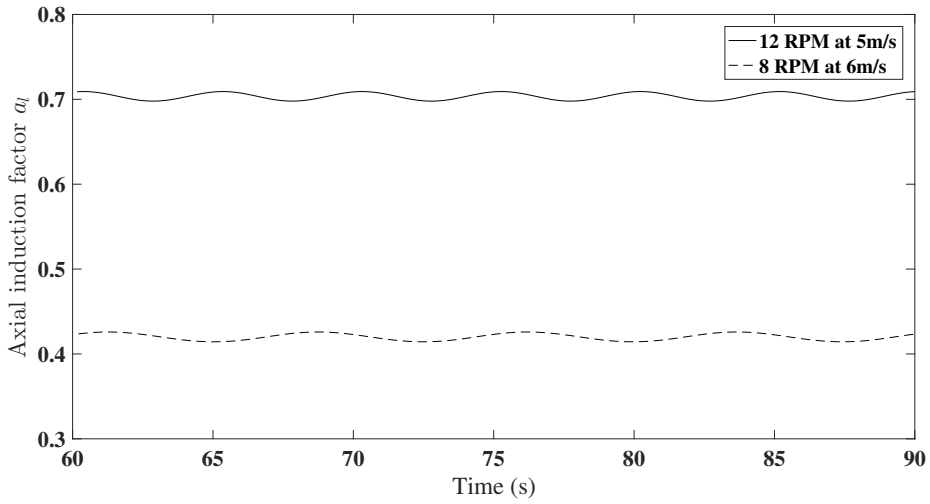

Figure 5.8: Axial induction factors, at 90% span, for an NREL 5MW reference turbine. The solid line represesnts a_l when wind velocity is $5m/s$ at $12.1RPM$, while the dashed line shows a_l for wind velocity $6m/s$ at $8.04RPM$.

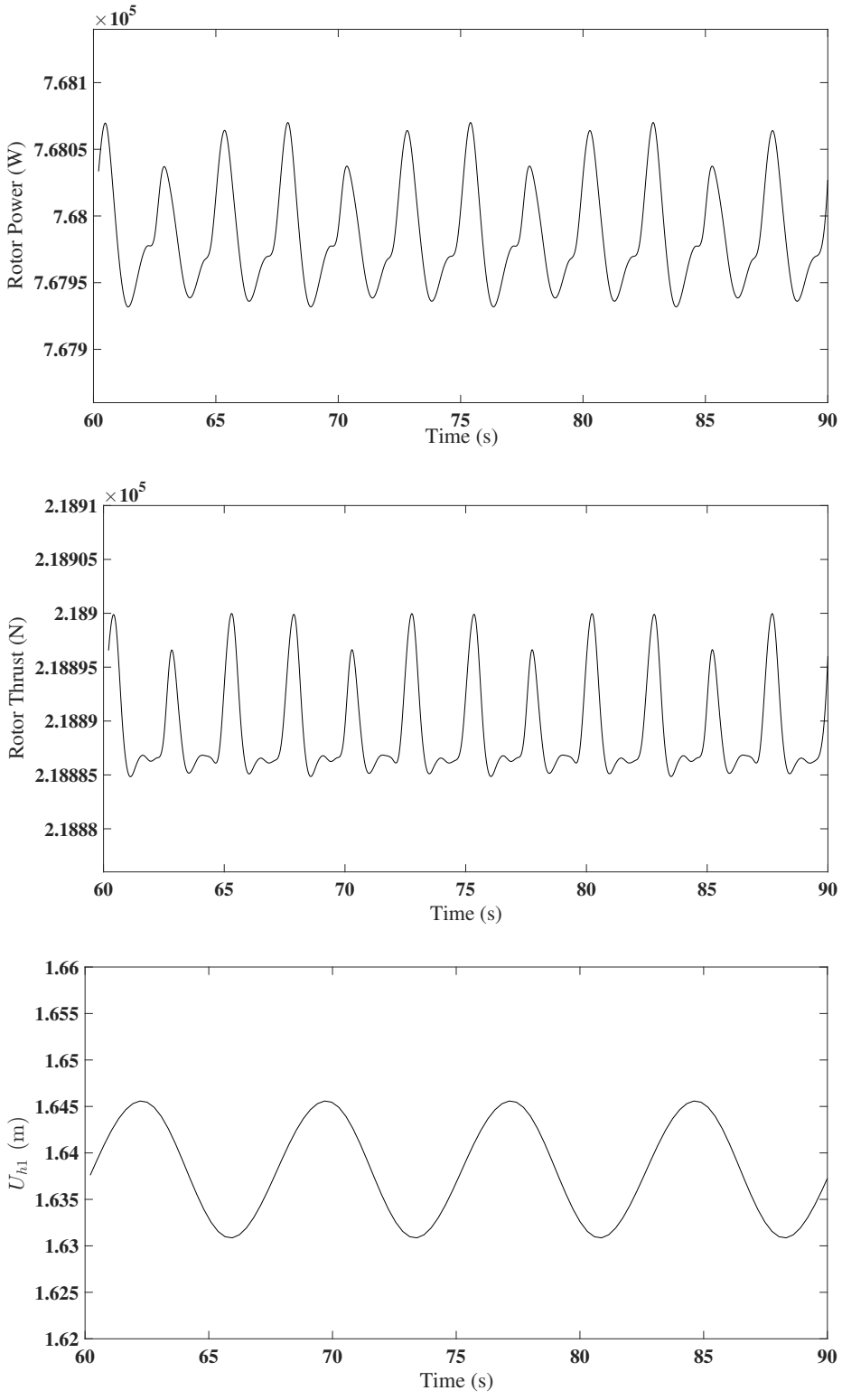

Figure 5.9: Power, thrust and blade displacement at 90% span for the start up zone of a rotor, with wind velocity at $6m/s$ and rotor at $8.04RPM$.

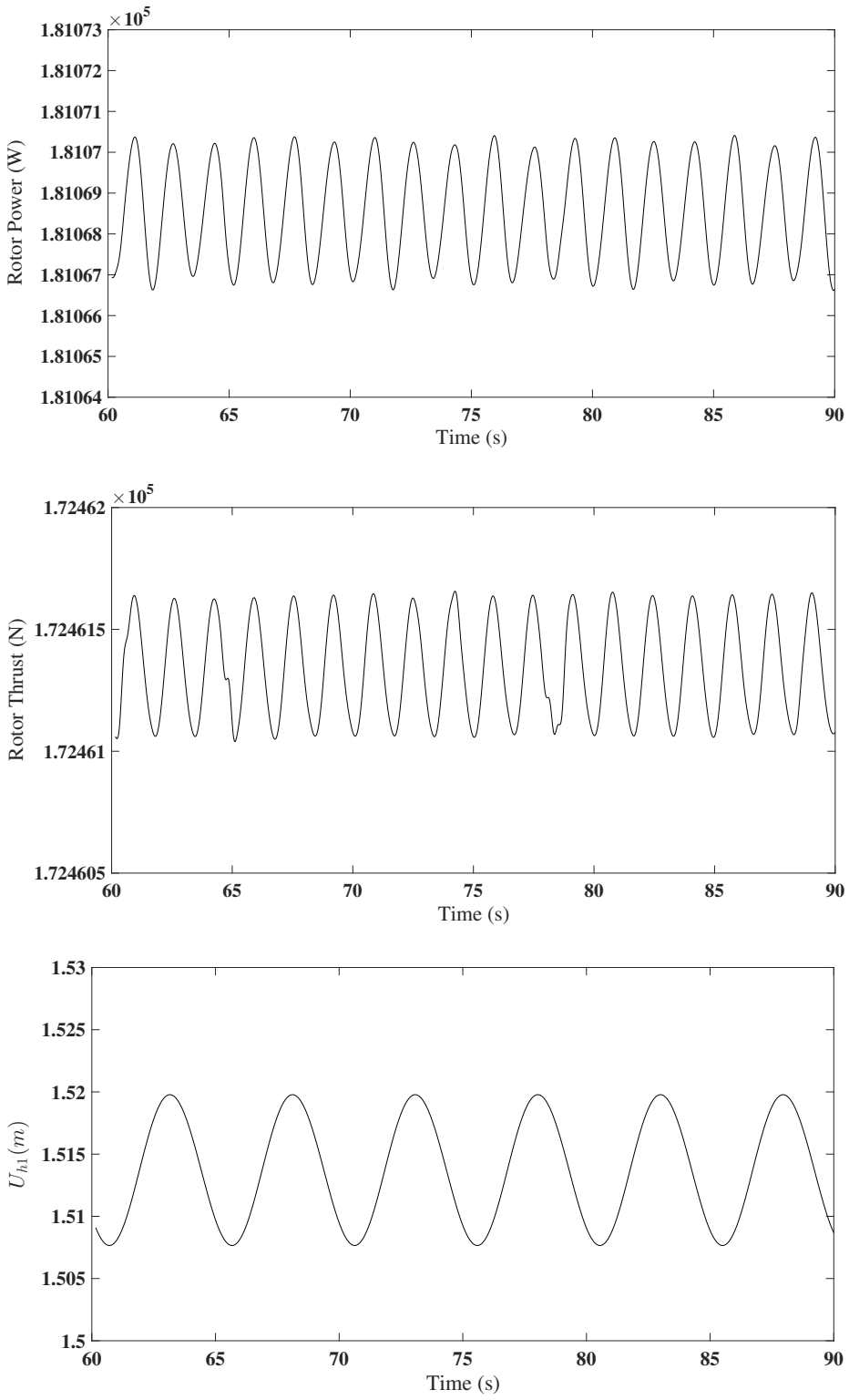

Figure 5.10: Power, thrust and blade displacement at 90% span when the wind velcity drops suddenly to $5m/s$ with the rotor still operating at $12.1RPM$.

Chapter 6

Conclusions

The results presented in Chapter 4 emphasize the 3-D DRD-BEM model's ability to capture the 3-Dimensional nature of interference patterns which become more and more significant as levels of misalignment in modern rotors increases. This increase in misalignment with the plane of rotation due to large scale deformation of blade sections increases the contribution of radial forces in the exchange of momentum with incoming wind. The tests presented in this research used progressively lighter and more flexible blades in addition to increasing hub-coning angles. This was done to methodically introduce misalignments into the rotor geometry, and observe how the new model performed under these test conditions. The results so obtained were analyzed and also compared with validated experiments from (Ponta et al. [8]) which in turn had used the standard DRD-BEM model.

Figures 4.1 and 4.2 help illustrate this notion of increased radial contribution by using just the increase in θ_{cn} in order to introduce misalignments. Since the blades used in the simulation that gave those plots were hyper-stiff, conicity was the only source of misalignments. Figure 4.1 shows how power extracted from the wind when computed using results from the 3-D DRD-BEM model shows a significant decrease in value. This is in accordance with the reasoning that the momentum balance equation, when looked at from the level of the hub-coordinate system, is more complete in 3-D DRD-BEM since it inlcudes all three force components affecting the change in momentum. The figure also shows that as the misalignments increased the difference in power computed by the two models goes up proportionally. This confirms the conlcusion that as the rotor operates more and more out-of-plane radial forces become increasingly important in the interference model. Figure 4.2 helps explain the above mentioned importance of radial forces by a comparison of the proportional influence of radial and tangential force components in terms of interference/induction factors. The radial induction factor a'' is comparable to the tangential induction factor a' under normal conditions suggesting that they are as important as a' in the iterative algorithm used for computing the induction factors. Moreover, in case of higher levels of misalignments, brought about by increasing θ_{cn}, a'' even exceeds a', thereby, highlighting its significance in modern wind turbines.

Figure 4.1 shows results of experiments where misalignments were introduced both by increasing θ_{cn} and by introducing blade flexibilty. The complex results justify use

of hyper-stiff blades at first in figures 4.1 and 4.2 to help understand the effects of misalignment in a step by step fashion. All types of blades, whether stiff or flexible, show the expected trend of a reduced rotor power obtained by the 3-D DRD-BEM model. Both models also show a drop in power for more flexible blades. This is due to increasingly complex modes of deformation, expected of flexible blades, captured by the advanced BEM models (see Ponta et al. [8] for an explanation with respect to the standard DRD-BEM model). The difference in power obtained by the two methods when looked at in proportion to the extent of misalignments is clearly different when the blades are flexible as opposed to when they are stiff. In stiff blades the difference is maximum in cases with higher θ_{cn} while for the flexible blades the difference is highest when $\theta_{cn} = 0$. This was, as explained in section 4.2,due to misalignments due to coning countering those due to blade deformation. While the tip displacement clearly increases for both models with increase in θ_{cn}, in case of the 3-D DRD-BEM model, the curves begin to flatten and eventually begin to increase in the region between 2.5° and 10° as blade flexibility increases. The curves from the standard model for different flexibilities, however, remain parallel in that region. This is an indication of the improved sensitivity of the 3-D DRD-BEM to the complex deformation modes.

The above mentioned notion of the 3-D DRD-BEM model being more sensitive to deformation can be best observed in the time dependent solutions shown in figures 4.4 and 4.5. Oscillations in the instantaneous response clearly have a higher amplitude for the new model when compared with the standard DRD-BEM model. This becomes

more evident with an increase in blade flexibility. Along the lines of previous results of the steady state solution there was a noticeable reduction in the mean value of all the variables shown in figures 4.4 to 4.7. As expected, including gravity to the mix leads to relative decrease in the impact of the change in aerodynamic loads brought about by the new model. Still, the mean value is noticeably lower for the 3-D DRD-BEM model. Thus, the 3-dimensional effects have a significant effet on the interference patterns across a stream tube.

The 3-D DRD-BEM will give a more comprehensive solution to the simulation of future turbines. This is based on the expectations that the future of wind turbines lies in implementing innovative control strategies which introduce higher levels of miaslignments than what is seen in the relatively stiff blades in use today. Since this new model can represent the aeroelastic effects of out-of-plane misalignments with higher accuracy and sensitivity it is ideally suited for testing active control actions like coning and pitching as well as passive control strategies like adaptive blades with bend-twist coupling. Advanced designs consisting of lighter and more flexible blades that will bring down cost of manufacturing along with those of transport-assembly will also lead to much higher levels of misalignments, further justifying the use of the 3-D DRD-BEM model.

Chapter 5 presents a much needed exploration of the high axial induction factor flow states with the help of numerical experiments. With a dramatic increase in the

complexity of control strategies the operational regimes of wind turbines has seen a sea of change. Turbines can now be expected to operate at high axial factor regimes for a much longer duration than seen earlier. Figures 5.1 show a 3-D DRD-BEM method used for modeling quite reasonable practical scenarios where the wind turbine can enter such flow states. These operational regimes should, thus, be taken seriously in all future Wind turbine models. Another reason for exploring these operational regimes is the 3-Dimensional effects of rotor misalignments on the aerodynamic forces as captured by 3-D DRD-BEM. That combined with the fact the 3-D DRD-BEM operates in the l coordinates system, thereby, as explained earlier, is bound to see higher values of axial induction factors especially at higher degrees of misalignments.

The $k-\epsilon$ turbulent flow analysis of an Actuator Disk model shows good agreement when compared with the results of Glauert's experimental data set, and is in excellent agreement with the theoretical curve in the region where the stream-tube control volume theory is valid (i.e. in the range of $a = 0$ to $a = 0.3$). Comparing figure 5.2 with figure 5.6, it can be seen that both sets of data clearly depart from the theoretical curve at around $a = 0.3$, and the spike in CT seen in figure 2.13 in the experimental data coincides with the first signs of wake recirculation seen in the Turbulence model (see figure 5.4 and the associated discussion); both occur at around $a = 0.4$, which also confirms the validity of the polynomial fit proposed here.

A new 4^{th} order polynomial was used to fit the new set of data as obtained by the

turbulent analysis, and this polynomial was used to find the CT for axial induction factors greater than 0.28. It is important to point out that Glauert's data do not cover the vortex ring state, which starts around $a = 0.9$. This was another motivation for performing this numerical analysis which extends to cover the region upto $a = 1.5$. Hence, this new model accomodates situations beyond $a = 0.9$, something which was lacking in previous BEM models. This operating regime will gain more importance as turbines are allowed to operate at much higher RPMs at part load conditions to store energy for wind farms in a "flywheel" mode. Thus, the numerical analysis presented here covers an importnat gap in the available data. Some other examples of experiments along these lines (e.g., [77, 78, 79, 80, 81] mostly concentrate on wake analysis and not on conditions at or around the disk, which is what is required in a BEM analysis.

As an outlook for further work, it would be useful to revisit the current implementation of the tip-hub loss factor, since the derivation proposed by Prandtl [82], as mentioned earlier, is based on a classical rotor aligned with the plane of rotation. It would, therefore, be a useful endeavour to reinterpret the tip-hub losses keeping sectional misalignments and heavy loading in mind and possibly come up with a modified expression.

References

[1] Davison, O.G.. Building smarter wind turbines: Eric Loth thinks like the wind. Popular Science; 2015. URL http://www.popsci.com/eric-loth-thinks-wind.

[2] Burton, T., Sharpe, D., Jenkins, N., Bossanyi, E.. Wind Energy Handbook. Chichester, UK: Wiley; 2001.

[3] IEC, . Wind turbine generator systems – part 13: Measurement of mechanical loads. Report IEC/TS 61400–13; International Electrotechnical Commission (IEC); 2001.

[4] Glauert, H.. The analysis of experimental results in the windmill brake and vortex ring states of an airscrew. Tech. Rep. Reports and Memoranda Volume 1026; Great Britain Aeronautical Research Committee; 1926.

[5] Buhl, M.. A new empirical relationship between thrust coefficient and induction

factor for the turbulent windmill state. Tech. Rep.; National Renewable Energy Laboratory; 2005.

[6] Lock, B., Townend, . An extension of the vortex theory of airscrews with applications to airscrews of small pitch, including experimental results. Aeronautical Research Committee, R&M 1925;1014(1014):1 to 49.

[7] Munk, M.M.. Model tests on the economy and effectiveness of helicopter propellers, naca tn 221 1925;.

[8] Ponta, F.L., Otero, A.D., Lago, L.I., Rajan, A.. Effects of rotor deformation in wind-turbine performance: The dynamic rotor deformation blade element momentum model (drd–bem). Renewable Energy 2016;92:157–170.

[9] Eggleston, D.M., Stoddard, F.. Wind turbine engineering design. Van Nostrand Reinhold Co. Inc., New York, NY; 1987.

[10] Walker, S.N.. Performance and optimum design analysis/computation for propeller type wind turbines. Ph.D. thesis; Oregon State University; 1976.

[11] Lock, C.N.H., Bateman, H., Townsend, H.C.H.. An extension of the vortex theory of airscrews with applications to airscrews of small pitch, including experimental results, reports and memoranda no. 1014. British Aeronautical Research Committee 1926;.

[12] Yu, W., Hodges, D.H., Volovoi, V., Cesnik, C.E.S.. On Timoshenko-like modeling of initially curved and twisted composite beams. Int J Sol and Struct 2002;39:5101–5121.

[13] Chen, L., Ponta, F.L., Lago, L.I.. Perspectives on innovative concepts in wind-power generation. Energy for Sustainable Development 2011;15:398–410.

[14] Hodge, N., Stocks, G.C.. Wind energy companies: A snapshot of the global wind industry. 2008. URL `www.greenchipstocks.com`.

[15] EWEA, . Upwind: Design limits and solutions for very large wind turbines. 2011. Sixth Framework Programme, European Wind Energy Association, Brussels, Belgium.

[16] Ponta, F.L., Otero, A.D., Rajan, A., Lago, L.I.. The adaptive-blade concept in wind-power applications. Energy for Sustainable Development 2014;22:3–12.

[17] Jamieson, P.. Innovation in wind turbine design. Wiley; 2011.

[18] Crawford, C., Platts, J.. Updating and optimization of a coning rotor concept. Journal of Solar Energy Engineering 2008;130:031002.

[19] Rasmussen, F., Petersen, J.T., Volund, P., Leconte, P., Szechenyi, E., Westergaard, C.. Soft rotor design for flexible turbines. Final report. Riso National Laboratory; 1998.

[20] Ichter, B., Steele, A., Loth, E., Moriarty, P., Selig, M.. A morphing downwind-aligned rotor concept based on a 13-mw wind turbine. Wind Energy 2016;19(4):625–637.

[21] Loth, E., Steele, A., Ichter, B., Selig, M., Moriarty, P.. Segmented up-a rotor for extreme-scale wind turbines. AIAA Aerospace Sciences Meeting 2012;1290.

[22] Crawford, C.. Re-examining the precepts of the blade element momentum theory for coning rotors. Wind Energy 2006;9(5):457–478.

[23] Bazilevs, Y., Hsu, M.C., Akkerman, I., Wright, S., Takizawa, K., Henicke, B., et al. 3d simulation of wind turbine rotors at full scale. part i: Geometry modeling and aerodynamics. International Journal for Numerical Methods in Fluids 2011;65(1-3):207–235.

[24] Bazilevs, Y., Hsu, M.C., Kiendl, J., Wuchner, R., Bletzinger, K.U.. 3d simulation of wind turbine rotors at full scale. part ii: Fluid-structure interaction modeling with composite blades. International Journal for Numerical Methods in Fluids 2011;65(1-3):236–253.

[25] Hansen, M.O.L., Sørensen, J.N., Vousitas, S., Sørensen, N., Madsen, H.A.. State of the art in wind turbine aerodynamics and aeroelasticity. Prog in Aerospace Sciences 2006;42:285–330.

[26] Jonkman, J.M., Buhl Jr, M.L.. Fast user's guide. Tech. Rep. NREL/EL-500-38230; National Renewable Energy Laboratory (NREL); Golden, Colorado, USA; 2005.

[27] Moriarty, P., Hansen, A., (US), N.R.E.L., Engineering, W.. Aerodyn theory manual. National Renewable Energy Laboratory; 2005.

[28] Laino, D., Hansen, A.. User's guide to the wind turbine aerodynamics computer software aerodyn. Tech. Rep.; National Renewable Energy Laboratory under subcontract No. TCX-9-29209-01; 2002.

[29] Otero, A.D., Ponta, F.L.. Structural analysis of wind-turbine blades by a generalized Timoshenko beam model. Journal of Solar Energy Engineering 2010;132:011015.

[30] Muljadi, E., Butterfield, C.P.. Pitch-controlled variable-speed wind turbine generation. IEEE Transactions on Industry Applications 2001;37(1):240–246.

[31] Geng, H., Yang, G.. Linear and nonlinear schemes applied to pitch control of wind turbines. The Scientific World Journal 2014;2014.

[32] Dvorkin, Y., Ortega-Vazuqez, M., Kirschen, D.. Wind generation as a reserve provider. Generation, Transmission Distribution, IET 2015;9(8):779–787.

[33] Sun, Y.Z., Zhang, Z.S., jie Li, G., Lin, J.. Review on frequency control

of power systems with wind power penetration. In: Power System Technology (POWERCON), 2010 International Conference on. 2010, p. 1–8.

[34] Lubosny, Z., Bialek, J.W.. Supervisory control of a wind farm. Power Systems, IEEE Transactions on 2007;22(3):985–994.

[35] Tang, X., Fox, B., Li, K.. Reserve from wind power potential in system economic loading. Renewable Power Generation, IET 2014;8(5):558–568.

[36] Muljadi, E., Singh, M., Gevorgian, V.. Fixed-speed and variable-slip wind turbines providing spinning reserves to the grid. In: Power and Energy Society General Meeting (PES), 2013 IEEE. 2013, p. 1–5.

[37] Erlich, I., Wilch, M.. Primary frequency control by wind turbines. In: Power and Energy Society General Meeting, 2010 IEEE. IEEE; 2010, p. 1–8.

[38] Sebastian, T.. The aerodynamics and near wake of an offshore floating horizontal axis wind turbine. Ph.D. thesis; University of Massachusetts - Amherst; 2012.

[39] Lock, C.N.H., Bateman, H.. Some experiments on airscrews at zero torque, with applications to a helicopter descending with engine "off", and to the design of windmills, reports and memoranda no. 885. British Aeronautical Research Committee 1924;.

[40] Wilson, R.E.. Aerodynamic behavior of wind turbines. In: Spera, D., editor.

Wind Turbine Technology, Fundamental Concepts of Wind Turbine Engineering. ASME Press, New York; 1994, p. 215–282.

[41] Jonkman, J., Butterfield, S., Musial, W., Scott, G.. Definition of a 5-MW reference wind turbine for offshore system development. Tech. Rep. NREL/TP-500-38060; National Renewable Energy Laboratory; 2009.

[42] Glauert, H.. Airplane propellers. In: Aerodynamic theory. Springer; 1935, p. 169–360.

[43] Manwell, J.F., McGowan, J.G., Rogers, A.L.. Wind energy explained: Theory, design and application. Chichester, UK: Wiley; 2002.

[44] Lanzafame, R., Messina, M.. Fluid dynamics wind turbine design: Critical analysis, optimization and application of {BEM} theory. Renewable Energy 2007;32(14):2291 – 2305.

[45] Lanzafame, R., Messina, M.. {BEM} theory: How to take into account the radial flow inside of a 1-d numerical code. Renewable Energy 2012;39(1):440 – 446.

[46] Madsen, H.A., Mikkelsen, R., Oye, S., Bak, C., Johansen, J.. A detailed investigation of the blade element momentum (bem) model based on analytical and numerical results and proposal for modifications of the bem model. In: Journal of Physics: Conference Series; vol. 75. IOP Publishing Ltd; 2007, p. 012016.

[47] Dai, J., Hu, Y., Liu, D., Long, X.. Aerodynamic loads calculation and analysis for large scale wind turbine based on combining {BEM} modified theory with dynamic stall model. Renewable Energy 2011;36(3):1095 – 1104.

[48] G., L.J., S., B.T.. A generalised model for airfoil unsteady aerodynamic behaviour and dynamic stall using the indicial method. In: 42nd. Annual Forum of the American Helicopter Society, Washington D. C. 1986,.

[49] Vaz, J.R.P., Pinho, J.T., Mesquita, A.L.A.. An extension of {BEM} method applied to horizontal-axis wind turbine design. Renewable Energy 2011;36(6):1734 – 1740.

[50] Griffin, D.A.. Blade system design studies volume I: Composite technologies for large wind turbine blades. Report SAND2002-1879; Sandia National Laboratories; 2002.

[51] Hodges, D.H.. Nonlinear Composite Beam Theory. Reston, Virginia: AIAA; 2006.

[52] Rankine, W.J.M.. On the Mechanical Priciples of the Action of Propellers. Institution of Naval Architects; 1865.

[53] Froude, W.. On the elementary relation between pitch, slip, and propulsive efficiency. Transactions of the Institute of Naval Architects 1878;19.

[54] Froude, R.E.. On the part played in propulsion by differences of fluid pressure. Transactions of the Institute of Naval Architects 1889;30(390-405):22.

[55] Hansen, M.. Aerodynamics of wind turbines. Earthscan/James & James; 2008.

[56] Du, Z., Selig, M.S.. A 3-D stall-delay model for horizontal axis wind turbine performance prediction. In: AIAA, Aerospace Sciences Meeting and Exhibit 36th, and 1998 ASME Wind Energy Symposium, Reno, Nevada, USA. American Institute of Aeronautics and Astronautics, ASME International; 1998, p. 9–19.

[57] Eggers, A.J.. Modeling of yawing and furling behavior of small wind turbines. In: 2000 ASME Wind Energy Symposium, 19 th, AIAA, Aerospace Sciences Meeting and Exhibit, 38 th, Reno, NV. 2000, p. 1–11.

[58] Leishman, J., Aerodynamicist, S., Beddoes, T., Specialist, A.. A Semi-Empirical Model for Dynamic Stall. Journal of the American Helicopter Society 1989;34:3.

[59] Leishman, J., Beddoes, T.. A generalized model for unsteady aerodynamic behaviour and dynamic stall using the indicial method. Journal of the American Helicopter Society 1990;36:14–24.

[60] Viterna, L.A., Janetzke, D.C.. Theoretical and experimental power from large horizontal-axis wind turbines. Tech. Rep.; National Aeronautics and Space Administration, Cleveland, OH (USA). Lewis Research Center; 1982.

[61] Prandtl, L.. Applications of modern hydrodynamics to aeronautics 1923;.

[62] Bak, C., Aagaard Madsen, H., Johansen, J.. Influence from blade-tower interaction on fatigue loads and dynamic (poster). In: Wind energy for the new millennium. Proceedings. 2001 European wind energy conference and exhibition (EWEC'01). 2001, p. 2–6.

[63] Powles, S.R.J.. The effects of tower shadow on the dynamics of a horizontal-axis wind turbine. Wind Engineering 1983;7:26–42.

[64] Xudong, W., Shen, W.Z., Zhu, W.J., Srensen, J.N., Jin, C.. Shape optimization of wind turbine blades. Wind Energy 2009;12(8):781–803.

[65] Burden, R.L., Faires, J.D.. Numerical analysis. Brooks Cole; 1998.

[66] Mathews, J.H., Fink, K.D.. Numerical methods using Matlab. Prentice Hall; 1999.

[67] Ahmadyar, A.S., Verbič, G.. Coordinated operation strategy of wind farms for frequency control by exploring wake interaction. IEEE Transactions on Sustainable Energy 2017;8(1):230–238.

[68] Venne, P., Guillaud, X., Teodorescu, R., Mahseredjian, J.. Generalized gain scheduling for deloaded wind turbine operation. Wind Engineering 2010;34(2):219–239.

[69] Stoddard, F.. Momentum theory and flow states for windmills. Wind Technology Journal, vol 1, Spring, 1977, p 3-9 1978;1:3–9.

[70] Stoddard, F.S.. Discussion of momentum theory for windmills. Tech. Rep.; University of Massachusetts - Amherst; 1976.

[71] Wilson, R.E., Lissaman, P.B.. Applied aerodynamics of wind power machines. Tech. Rep.; Oregon State Univ., Corvallis (USA); 1974.

[72] Sørensen, J.N., Shen, W.Z., Munduate, X.. Analysis of wake states by a full-field actuator disc model. Wind Energy 1998;1(2):73–88.

[73] Johnson, W.. Model for vortex ring state influence on rotorcraft flight dynamics. 4th american helicopter society decennial specialists conference on aeromechanics. San Francisco, CA, USA 2004;:21–23.

[74] ANSYS, I.. Ansys fluent theory guide release 15.0. 2013.

[75] Menter, F.R.. Zonal two equation k-turbulence models for aerodynamic flows. AIAA paper 1993;2906:1993.

[76] Shih, T.H., Liou, W.W., Shabbir, A., Yang, Z., Zhu, J.. A new k-elunate eddy viscosity model for high reynolds number turbulent flows. Computers and Fluids 1995;24(3):227–238.

[77] Castro, I.. Wake characteristics of two-dimensional perforated plates normal to an air-stream. Journal of Fluid Mechanics 1971;46(03):599–609.

[78] Hong, V.W.. Analysis of an Actuator Disc under Unsteady Loading: Validation of Engineering Models using Experimental and Numerical Methods. Master's thesis; Delft University of Technology and Technical University of Denmark; 2015.

[79] Lignarolo, L., Ragni, D., Ferreira, C.S., Van Bussel, G.. Kinetic energy entrainment in wind turbine and actuator disc wakes: an experimental analysis. In: Journal of Physics: Conference Series; vol. 524. IOP Publishing; 2014, p. 012163.

[80] Batten, W.M., Harrison, M., Bahaj, A.. Accuracy of the actuator disc-rans approach for predicting the performance and wake of tidal turbines. Phil Trans R Soc A 2013;371(1985).

[81] Harrison, M., Batten, W., Myers, L., Bahaj, A.. Comparison between cfd simulations and experiments for predicting the far wake of horizontal axis tidal turbines. IET Renewable Power Generation 2010;4(6):613–627.

[82] Betz, A.. Schraubenpropeller mit geringstem energieverlust. mit einem zusatz von l. prandtl. Nachrichten von der Gesellschaft der Wissenschaften zu Göttingen, Mathematisch-Physikalische Klasse 1919;1919:193–217.

Appendix A

Actuator Disk turbulent flow analysis results

Table A.1
Axial induction factor a given by the $k-\epsilon$ turbulence model for the pressure drop Δp applied across the disk. Δp is calculated based on the required CT value at the disk. W_2 is velocity at the disk.

$\Delta p\ [Pa]$	CT	$W_2\ m/s$	a
0.1225	0.2	0.9460554	0.0539446
0.18375	0.3	0.9164468	0.0835532
0.245	0.4	0.8845438	0.1154562
0.30625	0.5	0.8497124	0.1502876
0.3675	0.6	0.8101868	0.1898132

Continued on next page...

Table A.1 – Continued

$\Delta p\ [Pa]$	CT	$W_2\ m/s$	a
0.42875	0.7	0.7657464	0.2342536
0.49	0.8	0.7184002	0.2815998
0.55125	0.9	0.6642122	0.3357878
0.581875	0.95	0.6339225	0.3660775
0.6125	1	0.595845	0.404155
0.618625	1.01	0.5863391	0.4136609
0.62475	1.02	0.5759832	0.4240168
0.643125	1.05	0.545177	0.454823
0.655375	1.07	0.526983	0.473017
0.667625	1.09	0.4862064	0.5137936
0.67375	1.1	0.4780821	0.5219179
0.686	1.12	0.460547	0.539453
0.7105	1.16	0.4140027	0.5859973
0.735	1.2	0.3656748	0.6343252
0.784	1.28	0.2450877	0.7549123
0.79625	1.3	0.2235711	0.7764289
0.82075	1.34	0.1971868	0.8028132

Continued on next page...

Table A.1 – Continued

$\Delta p\ [Pa]$	CT	$W_2\ m/s$	a
0.8575	1.4	0.1713448	0.8286552
0.91875	1.5	0.1222184	0.8777816
0.98	1.6	0.08404594	0.91595406
1.04125	1.7	0.05170799	0.94829201
1.1025	1.8	0.02824944	0.97175056
1.47	1.9	−0.00605777	1.00605777
1.53125	2	−0.03325586	1.03325586
1.715	2.2	−0.08334035	1.08334035
1.96	2.4	−0.1279512	1.1279512
2.26625	2.5	−0.1513021	1.1513021
2.45	2.8	−0.2185324	1.2185324
2.75625	3.2	−0.3064317	1.3064317
3.0625	3.7	−0.4068528	1.4068528
6.125	4	−0.4653117	1.4653117

Appendix B

Copyright agreements

B.1 Copyright statement for figure 1.3

Figure 1.3 from chapter 1 is reproduced from *Wikimedia Commons*, a freely licensed media file repository. Files are licensed under the Creative Commons Attribution-Share Alike 2.0 and/or 3.0 Unported license. According to these license, permission is granted to:

1. Share, copy, distribute and transmit the work.

2. Remix, adapt the work.

Under the following conditions:

1. Attribution You must attribute the work in the manner specified by the author or licensor (but not in any way that suggests that they endorse you or your use of the work).

2. share alike If you alter, transform, or build upon this work, you may distribute the resulting work only under the same or similar license to this one.

ATTRIBUTIONS:

† Picture from figure 1.3 was taken by Hans Hillewaert. Source and permissions availables at: `http://en.wikipedia.org/wiki/File:Windmill_D1_(Thornton_Bank).jpg`, under CC-BY-SA-3.0.

B.2 Copyright statement for figure 1.1

Figure 1.1 from chapter 1 is reproduced from the Siemens' press release: https://www.siemens.com/press/IM2015050765WPEN under the following terms of use:

Press Pictures: Copyright

Siemens press photos may only be used for editorial purposes. All copyrights belong to Siemens AG, Munich/Berlin, unless another copyright is expressly given. Copyrights remain undiminished if the pictures are incorporated into an archive, either electronically or manually. Pictures used for editorial purposes, modified, duplicated and/or electronically altered must bear the credit "'. Commercial use or sale of the pictures and data, even in electronically manipulated form, is prohibited.

Specific restrictions regarding the use of the pictures could arise from the picture caption.

The photos may be printed free of charge, but in the case of print media we would appreciate a copy for our records. If pictures are used in films or electronic media, brief notification would suffice.

Email:

presspictures.cc@siemens.com

Postal address:

Publicis Pixelpark

Picturedesk

Implerstrae 11

81371 Munich

Germany

B.3 Permission to use figure 1.2

Michigan Tech

Anurag Rajan <arajan@mtu.edu>

Permission to use image
3 messages

Anurag Rajan <arajan@mtu.edu> Mon, Jul 11, 2016 at 10:45 AM
To: trevj@trevorjohnston.com

Hello,

I am currently working on a paper concerned with wind turbine research as part of my PhD dissertation. I was hoping to use the following image from a 2015 news article in Popular Science -

http://www.popsci.com/sites/popsci.com/files/styles/large_1x_/public/wind-turbines-hiw_0.jpg?itok=9HL6EseU

This image is from the report titled "Building Smarter Wind Turbines - Eric Loth thinks like the wind" dated May 20, 2015, by Osha Gray Davison.

(link - http://www.popsci.com/eric-loth-thinks-wind).

I have already contacted both Popular Science and Dr. Eric Loth, and was directed to you for permission to use that image. I would really appreciate it if I could get permission to re-use that image as it would greatly enhance the quality of my journal submission and subsequently my PhD dissertation.

Thanks & regards,
Anurag Rajan
Graduate Student
Michigan Technological University

Trevor Johnston <trevj@trevorjohnston.com> Mon, Jul 11, 2016 at 11:04 AM
To: Anurag Rajan <arajan@mtu.edu>

Hi Anurag,

Yes you're free to use the graphic for your paper. I just ask that you please credit trevorjohnston.com.

Regards,
Trevor

Sent from my iPhone
[Quoted text hidden]

Anurag Rajan <arajan@mtu.edu> Mon, Jul 11, 2016 at 11:16 AM
To: Trevor Johnston <trevj@trevorjohnston.com>

Thanks a lot Trevor. I really appreciate the quick response. I'll definitely credit you for that graphic.

Regards,
Anurag